J|A|C|S
ARTICLES
Published on Web 10/16/2004

Magnetic, Electronic, and Structural Characterization of Nonstoichiometric Iron Oxides at the Nanoscale

Franz X. Redl,[†,‡] Charles T. Black,[†] Georgia C. Papaefthymiou,[§] Robert L. Sandstrom,[†] Ming Yin,[‡] Hao Zeng,[†] Christopher B. Murray,*[,†] and Stephen P. O'Brien*[,‡]

Contribution from the T. J. Watson Research Center, Nanoscale Materials and Devices, IBM, 1101 Kitchawan Road, Route 134, P.O. Box 218, Yorktown Heights, New York 10598, Villanova University, 800 Lancaster Avenue, Villanova, Pennsylvania 19085, and Department of Applied Physics & Applied Mathematics, Columbia University, 200 SW Mudd Building, 500 West 120th Street, New York, New York 10027

Received May 29, 2004; E-mail: so188@columbia.edu; cbmurray@us.ibm.com

Abstract: We have investigated the structural, magnetic, and electronic properties of nonstoichiometric iron oxide nanocrystals prepared by decomposition of iron(II) and iron(0) precursors in the presence of organic solvents and capping groups. The highly uniform, crystalline, and monodisperse nanocrystals that were produced enabled a full structural and compositional survey by electron microscopy and X-ray diffraction. The complex and metastable behavior of nonstoichiometric iron oxide (wüstite) at the nanoscale was studied by a combination of Mössbauer spectroscopy and magnetic characterization. Deposition from hydrocarbon solvents with subsequent self-assembly of iron oxide nanocrystals into superlattices allowed the preparation of continuous thin films suitable for electronic transport measurements.

Introduction

The large contribution of surface energy in nanoscale materials can stabilize and favor the origin of phases which are not known or thermodynamically unstable in the bulk.[1−5] Synthetic control over the nanocrystal phase is therefore an additional degree of freedom in the search for new nanoscale materials properties. Furthermore, it allows to some extent the alteration of crystal shape[6,7] evolving in the growth period due to the surface-differentiating influence of capping groups. This can be exploited to obtain ellipsoids, sticks, rods,[8,9] or branched structures[10] of materials with internal hexagonal structure. Controlled growth of spherical particles with internal cubic symmetry can lead to truncated cubes, cubes, or star-shaped particles.[11] The target of our investigation was the synthesis and characterization of wüstite nanocrystals.[12,13]

We have investigated the structural, magnetic, and electronic properties of nonstoichiometric iron oxide nanocrystals prepared by decomposition of iron(II) and iron(0) precursors in the presence of organic solvents and capping groups. The highly uniform, crystalline, and monodisperse nanocrystals that were produced enabled a full structural and compositional survey by electron microscopy and X-ray diffraction. Different precursors and a selective oxidation method were explored for the synthesis of nanocrystalline wüstite (Fe_xO for $0.84 < x < 0.95$). Iron acetylacetonate, iron acetate, and iron pentacarbonyl were decomposed in organic solvents with high boiling temperatures. The size and shape of the reaction product are correlated to the metastability of wüstite. Tight control over temperature allows the syntheses of cubic or faceted Fe_xO nanocrystals with narrow size distributions by thermolysis of iron(II) acetate or a selective oxidation route of iron pentacarbonyl with pyridine *N*-oxide. Random aggregation of particles is initiated at higher reaction temperatures due to the disproportionation of the Fe_xO particles into magnetite and α-Fe. Structural characterization of the Wüstite nanocrystals prepared by these methods reveals incorporated small seeds of magnetite. Self-assembly of spherical Fe_xO nanocrystals yields well-known densely packed hexagonal or cubic superlattices, whereas the cubic nanocrystals assemble readily into simple cubic superlattices. The assembly process

* Correspondence and requests for materials should be addressed to Stephen O'Brien (synthesis and structural characterization) and/or Christopher B. Murray (magnetic and electronic characterization).
† IBM.
§ Villanova University.
‡ Columbia University.

(1) Ayyub, P.; Palkar, V. R.; Chattopadhyay, S.; Multani, M. *Phys. Rev. B* **1995**, *51*, 6135−6138.
(2) Herhold, A. B.; Chen, C.-C.; Johnson, C. S.; Tolbert, S. H.; Alivisatos, A. P. *Phase Transitions* **1999**, *68*, 1−25.
(3) Qadri, S. B.; Skelton, E. F.; Hsu, D.; Dinsmore, A. D.; Yang, J.; Gray, H. F.; Ratna, B. R. *Phys. Rev. B* **1999**, *60*, 9191−9193.
(4) Diehl, M. R.; Yu, J.-Y.; Heath, J. R.; Held, G. A.; Doyle, H.; Sun, S.; Murray, C. B. *J. Phys. Chem. B* **2001**, *105*, 7913−7919.
(5) Sun, S.; Murray, C. B. *J. Appl. Phys.* **1999**, *85*, 4325−4330.
(6) Jun, Y.-W.; Lee, S.-M.; Kang, N.-J.; Cheon, J. *J. Am. Chem. Soc.* **2001**, *123*, 5150−5151.
(7) Jun, Y.-w.; Jung, Y.-y.; Cheon, J. *J. Am. Chem. Soc.* **2002**, *124*, 615−619.
(8) Puntes, V. F.; Krishnan, K.; Alivisatos, A. P. *Top. Catal.* **2002**, *19*, 145−148.
(9) Puntes, V. F.; Krishnan, K. M.; Alivisatos, A. P. *Science (Washington, DC)* **2001**, *291*, 2115−2117.
(10) Manna, L.; Scher, E. C.; Alivisatos, A. P. *J. Am. Chem. Soc.* **2000**, *122*, 12700−12706.
(11) Lee, S.-M.; Jun, Y.-w.; Cho, S.-N.; Cheon, J. *J. Am. Chem. Soc.* **2002**, *124*, 11244−11245.
(12) Cornell, R. M.; Schwertmann, U. *The Iron Oxides*; John Wiley & Sons: New York, 1997.
(13) Yin, M.; O'Brien, S. *J. Am. Chem. Soc.* **2003**, *125*, 10180−10181.

can be directed by an external magnetic field, yielding needle-like structures or pillars. By annealing in inert or oxidizing atmospheres, the wüstite nanocrystals are transformed into high-quality magnetite or maghemite nanocrystals (observed by X-ray diffraction, SAED, and SQUID measurements). Intermediate transition states display interesting magnetic properties minted by exchange coupling between anti-ferromagnetic wüstite and ferrimagnetic magnetite. Magnetite/Fe particles obtained by the disproportionation of Fe_xO nanocrystals show magnetoresistance (MR) from 8% at 70 K to about 3% at room temperature.

Wüstite, Fe_xO (also spelled "wuestite" and sometimes "wustite"), is a nonstoichiometric phase with a known stability range from $x = 0.83$ to 0.96 above 560 °C. The phase is also know as $Fe_{1-y}O$ (here, $x = 1 - y$). Prior to structural investigations of iron oxides at the nanoscale, wüstite was typically prepared by heating iron and magnetite in sealed vessels, and was known to be stable only above 560−570 °C. Below this temperature it decomposes via a two-step mechanism into α-Fe and magnetite, Fe_3O_4.[12,14−16] Fe_xO has a defect rock salt structure with an ordered distribution of iron vacancies.[17−19] Fe_xO can be oxidized to magnetite and finally to maghemite, γ-Fe_2O_3. All three compounds are based on an approximately face-centered cubic structure of oxygen. One can readily visualize a fcc close-packed array of O^{2-} ions and the successive filling of the octahedral and tetrahedral sites that result. The transformation between the three different phases is thought to be determined by the diffusion of Fe^{2+} and Fe^{3+} ions within the oxygen sublattice and electron transfer between iron ions of different valence. The wealth of the system is enriched by the occurrence of non-stoichiometry in all three phases. It is also interesting to note that magnetite is the only thermodynamically stable phase in the bulk.[20]

The three iron oxides are marked by different properties. Fe_xO is paramagnetic at room temperature and antiferromagnetic or weakly ferrimagnetic[21,22] below the Néel temperature T_N of about 183 K[23] or 198 K,[24] due to a transition from the cubic to a rhombohedral[25] or a monoclinic structure.[14,15] The transition is strongly related to the defect structure of wüstite. Magnetite and maghemite are ferrimagnetic. Magnetite is half metallic and shows comparable high conductivity, which is based on electron exchange between Fe^{2+} and Fe^{3+}. The conductivity is thermally activated and undergoes a first-order transition at the Verwey[26] temperature at 120 K. The conductivity changes by orders of magnitude at this temperature. The appearance of this transition and the Verwey temperature are strongly correlated to the perfection of the magnetite crystal under investigation.

The aim of this study was to explore the ability of chemical methods to control size, morphology, and ultimately properties of the cubic iron oxides over a compositional range between Fe_xO and Fe_2O_3 with a focus on Fe_xO nanoparticles as the initial precursor nanocrystal to oxides of higher oxidation states.[27−29] Our interest in this material was triggered by the metastability of Fe_xO and the possibility of generating mixed phases between magnetite, iron, and wüstite. Our approach of breaking the synthesis down into a series of kinetically stable steps has yielded insight into the mechanism of formation of iron oxide nanocrystals, from precursor decomposition through nucleation and morpholigcal evolution. The metastability has been exploited to adjust the composition of the particles on a nanoscale size regime. This allows changing properties in a systematic and controlled way based on the relative amount of Fe_xO to Fe_3O_4/α-Fe and based on the influence of interfaces. Such systems are expected to show magnetic exchange coupling caused by interfaces between antiferromagnetic Fe_xO and the ferrimagnetic Fe_3O_4 leading to a shift in hystereses and increased coercivity.[30−32] Further, the conductivity of those mixed-phase nanoparticles assemblies might be spin dependent because of the interface between superparamagnetic nanocrystals and half-metallic properties of magnetite.[33−35] Finally, Fe_xO can be used as a nonmagnetic precursor, transferable into magnetite or maghemite. This is especially interesting because of the current restriction to mainly water-based syntheses that often yield materials with structural imperfections.[20,36,37]

In the following sections, the synthesis is outlined starting with the most effective reaction concerning the control over phase, phase purity, size, and shape. Those conditions were found in an evolutionary process of searching for the right precursors and reaction conditions. Results of earlier investigated reactions will also be presented in the main text (controlled oxidation with PyO) or in the Supporting Information (decomposition of Fe^{II}acac or Fe^{III}acac). We will also show that the quality of the obtained Fe_xO nanocrystals is related to the decomposition temperature of the precursor, reaction time, and to some extent the choice of surfactant and solvent.

Experimental Section

Chemicals. Iron(II) acetylacetonate ($Fe(acac)_2$), iron(III) acac ($Fe(acac)_3$), iron(II) acetate (Fe_xOAc_2), iron pentacarbonyl, trioctylamine (TOA), dioctyl ether (DOE), diphenyl ether (DPE), oleic acid (OA), lauric acid (LA), trioctylphosphine, tributylphosphine, trioctylphosphine oxide, hexane, acetone, and ethanol were purchased in high grade from

(14) Fjellvag, H.; Hauback, B. C.; Vogt, T.; Stolen, S. *Am. Mineral.* **2002**, *87*, 347−349.
(15) Fjellvag, H.; Gronvold, F.; Stolen, S.; Hauback, B. *J. Solid State Chem.* **1996**, *124*, 52−57.
(16) Stolen, S.; Gloeckner, R.; Gronvold, F. *Thermochim. Acta* **1995**, *256*, 91−106.
(17) Nagakura, S.; Ishiguro, T.; Nakamura, Y. Structure of wuestite observed by UHV−HR-1 MV electron microscope. Dept. Metall., Tokyo Institute of Technology, Tokyo, Japan, 1983.
(18) Radler, M. J. Thesis, Northwestern University, Evanston, IL, 1990; p 407.
(19) Gavarri, J. R.; Carel, C.; Weigel, D. *C. R. Acad. Sci., Ser. 2* **1988**, *307*, 705−710.
(20) Hyeon, T.; Lee, S. S.; Park, J.; Chung, Y.; Na, H. B. *J. Am. Chem. Soc.* **2001**, *123*, 12798−12801.
(21) Shull, C. G.; Strausser, W. A.; Wollan, E. O. *Phys. Rev.* **1951**, *83*, 333−345.
(22) Bizette, H.; Tzai, B. *Acad. Sci. Paris* **1943**, *217*, 390.
(23) Millar, R. W. *J. Am. Chem. Soc.* **1929**, *51*, 215.
(24) Schiber, M. M., Ed. *Experimental Magnetochemistry*; John Wiley & Sons: New York, 1967.
(25) Toombs, N. C.; Rooksby, H. P. *Nature (London)* **1950**, *165*, 442.
(26) Verwey, E. J. W. *Nature (London)* **1939**, *144*, 327.
(27) Ding, J.; Miao, W. F.; Pirault, E.; Street, R.; McCormick, P. G. *J. Magn. Magn. Mater.* **1998**, *177−181*, 933−934.
(28) Ding, J.; Miao, W. F.; Street, R.; McCormick, P. G. *Scr. Mater.* **1996**, *35*, 1307−1310.
(29) Gotor, F. J.; Macias, M.; Ortega, A.; Criado, J. M. *Phys. Chem. Miner.* **2000**, *27*, 495−503.
(30) Nogués, J.; Schuller, I. K. *J. Magn. Magn. Mater.* **1999**, *192*, 203−232.
(31) Lin, X.; Murthy, A. S.; Hadjipanayis, G. C.; Swann, C.; Shah, S. I. *J. Appl. Phys.* **1994**, *76*, 6543−6545.
(32) Gangopadhyay, S.; Hadjipanayis, G. G.; Shah, S. I.; Sorensen, C. M.; Klabundea, K. J. *J. Appl. Phys.* **1991**, *70*, 5888−5890.
(33) Poddar, P.; Fried, T.; Markovich, G. *Phys. Rev. B: Condens. Matter* **2002**, *65*, 172405.
(34) Black, C. T.; Murray, C. B.; Sandstrom, R. L.; Sun, S. *Mater. Res. Soc. Symp. Proc.* **2001**, *636*, D10.17/11−D10.17/15.
(35) Black, C. T.; Murray, C. B.; Sandstrom, R. L.; Sun, S. *Science (Washington, DC)* **2000**, *290*, 1131−1134.
(36) Rockenberger, J.; Scher, E. C.; Alivisatos, A. P. *J. Am. Chem. Soc.* **1999**, *121*, 11595−11596.
(37) Sun, S.; Zeng, H. *J. Am. Chem. Soc.* **2002**, *124*, 8204−8205.

Scheme 1. Different Reactions under Investigation for the Synthesis of Wüstite Nanocrystals

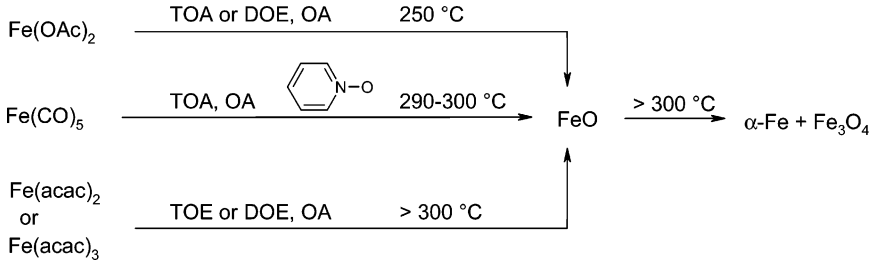

Aldrich. Pyridine *N*-oxide (PyO) and trimethyl *N*-oxide hydrate were purchased from Aldrich and dehydrated utilizing a Dean−Stark trap and toluene. After crystallization from hot toluene solution and isolation, the *N*-oxides were dried under vacuum and stored in a glovebox. The phosphines and phosphine oxide were also stored in the glovebox. An N_2 atmosphere was used for all reactions. Solvent and surfactant mixtures were generally preheated to 250 °C under a rapid N_2 flow over solvent for 20 min. As a byproduct, a black oily substance (amorphous polymeric material) is observed occasionally in small yields, removed by repeated careful precipitations of diluted hexane solutions with an equal volume of acetone.

Decomposition of Iron Pentacarbonyl in the Presence of Pyridine *N*-Oxide. In a typical reaction, 7.6 mmol of PyO and 3.02 mmol of iron pentacarbonyl are added subsequently to a solution of 9.12 mmol of LA in 14 mL of DOE at 100 °C. The clear solution is heated to 120 °C for 2 h. The light yellow solution color changes to dark red. After heating to reflux, in order to observe the evolution of size and shape, aliquots/fractions of the solution are extracted with a syringe at specified time intervals. Usually particles can be isolated after an induction period of about 30 min, whereupon the formation of product can be observed as a slight increase in brightness and turbidity of the solution. After cooling to room temperature, the black solution is precipitated with acetone. The precipitate is redispersed in hexane, and a surplus of 2 mL of OA is added in order to exchange lauric acid against the fatty acid. Insoluble fractions are removed by centrifugation or, if possible, with a magnet and decanting of the supernatant. The precipitation with acetone is repeated as well as the addition of oleic acid. This procedure is repeated until the supernatant is clear. The precipitation steps with acetone are necessary to remove byproducts (dark oil, polymer). Afterward the particles are redispersed in hexane and stored under nitrogen in a freezer.

Decomposition of Iron(II) Acetate. In a typical reaction, 8.0 mmol of $FeOAc_2$ is added to a solution of 2 mL of OA and 14−15 mL of TOA at room temperature. The dark dispersion is heated to 250 °C with a heating rate of about 10 °C min^{-1}. Around 200 °C, the dark dispersion clears and the color changes to light yellow, which changes again to black a few minutes after reaching 250 °C. The reaction is kept at 250 °C for an additional 20 min. Reaction temperature, time, and surfactant concentration can be varied to obtain small spherical, intermediate cubic, or larger faceted particles. The particles are precipitated by adding acetone or ethanol after cooling the reaction mixture to room temperature. The particles are separated and cleaned by repeated precipitation of the hexane solution with acetone or ethanol. Afterward the particles are redispersed in hexane and stored under nitrogen in a freezer.

Structural and Optical Characterization. Images of the particles were taken on a Phillips CM12 transmission electron microscope (TEM) in bright-field (BF) and dark-field (DF) mode at 120 kV. Samples were prepared by drying solvent dispersions of the nanoparticles onto Formvar amorphous carbon-backed 200 or 400 mesh grids and then drying under vacuum at 100 °C. Wide-angle and small-angle electron diffraction patterns were obtained in selected area electron diffraction mode (SAED), covering areas of ~1 μm in diameter. X-ray powder diffraction experiments were performed on a Siemans D-500 diffractometer using Co Kα radiation (λ = 1.78892 Å). Solvent dispersions of the nanoparticles were dried on glass substrates. FT-IR spectra of solution (thin-film cell) or solids (dispersed in KBr or dried on polymer film) were obtained with a Nikola FT-IR spectrometer. Optical images of superlattices on a glass or silicon substrate were obtained with a Nikon optical microscope.

Magnetic Characterization. FC (Field Cooled) and ZFC (Zero FC), and hystereses loops were measured utilizing a Quantum Design MPMS2 SQUID magnetometer and thin layers of iron oxide particles deposited on a silicon wafer by evaporation of the solvent (hexane). Transmission Mössbauer studies were conducted on a Ranger Electronics Mössbauer spectrometer equipped with a Janis Research Co. Super-Veritemp dewar and a Lakeshore Co. temperature controller, allowing sample temperature variation from 4.2 K to room temperature. The source was 50-mCi ^{57}Co in a Rh matrix, maintained at room temperature. The spectrometer was calibrated with a 7-μm-thick ^{57}Fe-enriched iron foil. Isomer shifts are referenced to metallic iron at room temperature. Spectral fits were performed using the program WMOSS (Web-Research Co). Samples were received in an inert atmosphere and stored at liquid nitrogen temperature until measured.

Results and Discussion

Synthesis and Reaction Chemistry. We have explored the synthesis of iron oxides over a range of compositions based on an underlying reaction scheme that relies on the decomposition of simple salts or organometallic precursors of Fe in high-boiling organic solvents in the presence of suitable surfactants. The surfactants affect the chemistry of the decomposition and control nanocrystal nucleation and growth in their capacity as ligands that reduce the surface energy of the crystal. This type of approach is well established in nanoscale syntheses.[38,39] By optimizing the reaction conditions, we can allow size-selective formation of solvent-dispersible materials.

To synthesize Fe_xO nanocrystals, different iron precursors [$Fe(CO)_5$, $Fe(acac)_2$, $Fe(acac)_3$, $Fe(OAc)_2$] were investigated (see Scheme 1). The decomposition of iron pentacarbonyl has found broad use in nanoscale syntheses.[20,40−43] Iron acetate salts have been used to generate nanostructured e.g. Ni,[44,45] PZT,[46] ZnO,[47] or rare earth metal oxides.[48] Iron(III) acac has been used for

(38) Scher, E. C.; Manna, L.; Alivisatos, A. P. **2003**, *361*, 241−255.
(39) Murray, C. B.; Kagan, C. R.; Bawendi, M. G. *Annu. Rev. Mater. Sci.* **2000**, *30*, 545−610.
(40) Park, S.-J.; Kim, S.; Lee, S.; Khim, Z. G.; Char, K.; Hyeon, T. *J. Am. Chem. Soc.* **2000**, *122*, 8581−8582.
(41) Caro, D. d.; Ely, T. O.; Mari, A.; Chaudret, B. *Chem. Mater.* **1996**, *8*, 1987−1991.
(42) Wonterghem, J. v.; Morup, S.; Charles, S. W.; Wells, S.; Villadsen, J. *Phys. Rev. Lett.* **1985**, *55*.
(43) Sun, S.; Murray, C. B.; Weller, D.; Folks, L.; Moser, A. *Science (Washington, DC)* **2000**, *287*, 1989−1992.
(44) Xia, B.; Lenggoro, I. W.; Okuyama, K. *Chem. Mater.* **2002**, *14*, 2623−2627.
(45) Ayyappan, S.; Rao, C. N. R. *Eur. J. Solid State Inorg. Chem.* **1996**, *33*, 737−749.
(46) Vorotilov, K. A.; Yanovskaya, M. I.; Turevskaya, E. P.; Sigov, A. S. *J. Sol-Gel Sci. Technol.* **1999**, *16*, 109−118.
(47) Audebrand, N.; Auffredic, J.-P.; Louer, D. *Chem. Mater.* **1998**, *10*, 2450−2461.

Table 1. Reaction Conditions of the Decomposition of $Fe(OAc)_2$ (4.0 mmol)

solvent (volume)	surfactant	*T*/°C	*t*/min	*a*/Å[a] *y*[b]	phase (crystal size[c])	observations, size, and shape (derived from TEM)
DPE, DOE, or TOA[d] (14 mL)	OA[e] (12 mmol)	250−290	120		Fe_3O_4 or γ-Fe_2O_3 (3.5 nm)	slow (temperature-dependent) reaction, 4−5 nm NC, 5% SD, oxidized during isolation
TOA (7 mL)	OA (6.0 mmol)	255	90	4.240 0.80	Fe_xO (10 nm) Fe_3O_4 (3−4 nm)	bimodal size distribution: minority of 5 nm small Fe_3O_4 particles (after oxidation in air) and majority of strongly faceted ellipsoidal Fe_xO NC with 14 nm (long axis)
TOA (7 mL)	OA (3.0 mmol)	255	10	4.229 0.78	Fe_xO (7 nm)	cubic (8 nm edge length, 12 nm diagonal length, SD 8%)
		255	25	4.247 0.82	Fe_xO (9 nm) Fe_3O_4 (3 nm)	cubic (11 nm edge length, 15 nm diagonal length, SD 7%)
		255	80	4.285 0.90	Fe_xO (12 nm) Fe_3O_4 (3 nm)	faceted particles (18 nm, SD 8%), truncated octahedrons
		255	140	4.289 0.90	Fe_xO (13 nm) Fe_3O_4 (5−6 nm)	faceted particles (19 nm), truncated and elongated octahedrons

[a] Cubic crystal cell length *a* calculated from {200} Bragg reflection for Fe_xO phase. [b] Calculated applying the formula $a(Å) = 3.856 + 0.478y$.[59] [c] Calculated from broadening of Bragg reflections in the X-ray pattern {Fe_3O_4, (311); α-Fe, (110); Fe_xO, (200)}. [d] DPE, DOE, and TOA are diphenyl ether, dioctyl ether, and trioctylamine, respectively. [e] OA is oleic acid.

Table 2. Reaction Conditions of the Decomposition of $Fe(CO)_5$ (3.02 mmol) in the Presence of PYO

solvent (volume)	oxidizer, surfactant	*T*/°C	*t*/min	*a*/Å[a] *y*[b]	phase (crystal size[c])	observations, size, and shape (derived from TEM)
DPE (14 mL)	PYO (15.2 mmol) LA (9.12 mmol)	256	100		Fe_xO	slow reaction, broad size distribution (10−60 nm), very diffuse electron diffraction pattern
TOA (14 mL)	PYO (12.6 mmol) LA (9.12 mmol)	350	60	4.275 0.88	Fe_xO (20 nm) a-Fe (22 nm) Fe_3O_4 (32 nm)	cubic or nearly cubic particles, size distributions centered around 30, 60, and 100 nm
TOA (14 mL)	PYO (15.2 mmol) LA (9.12 mmol)	296	60	4.292 0.91	Fe_xO (10 nm)	star shaped NC, 20−30 nm diameter and larger aggregates
TOA (14 mL)	PYO (15.2 mmol) LA (9.12 mmol)	296	20	4.286 0.90	Fe_xO (7 nm)	aggregates of small seeds of 8 nm
			60		Fe_xO Fe_3O_4 Fe	spherical, faceted Fe_xO particle (15 nm) and cubic particles (Fe_3O_4+Fe) with 40 nm diagonals
TOA (14 mL)	PYO (15.2 mmol) LA (9.1 mmol)	296	50	4.258 0.84	Fe_xO Fe_3O_4 Fe	spherical, faceted Fe_xO particle (15 nm) and cubic particles (Fe_3O_4 + Fe) with 40 nm diagonals
DOE (14 mL)	PYO (11.4.mmol) LA (9.1 mmol)	296	45		Fe_xO	cubes of 16 nm diagonal length
DOE (14 mL)	PYO (7.6 mmol) LA (9.1 mmol)	296	35	4.231 0.79	Fe_xO (9 nm)	cubes with diagonal length of 15 nm, 8% SD
			70	4.261 0.85	Fe_xO (10 nm)	cubes (less regular than after 35 min) with diagonal length of 17 nm
DOE (18.6 mL)	PYO (7.6 mmol) LA (9.1 mmol)	296	30		Fe_xO	faceted spheres of 12 nm diameter
		296	60		Fe_3O_4 (23 nm) α−Fe (23 nm)	large cubes or faceted particles about 30 nm
DOE (28 mL)	PYO (7.6 mmol) LA (9.1 mmol)	296	30 (90)		Fe_xO−Fe_3O_4	spherical particles of 8 nm (SD is increasing over time; particles up to 13 nm are observable later on)

[a] Cubic crystal cell length *a* calculated from {200} Bragg reflection. [b] Calculated with the formula $a(Å) = 3.856 + 0.478y$.[59] [c] Calculated from peak broadening of Bragg reflections in the X-ray pattern {Fe_3O_4, (311); α-Fe, (110); Fe_xO, (200)}.

film deposition[49−52] and recently to generate magnetite nanocrystals with sizes ranging from 4 to 20 nm by a seeded growth reaction.[37] Details of the reaction of iron acac compounds to form Fe_xO nanocrystals, with generally less control over size and extent of aggregation, are summarized briefly in the Supporting Information. Reaction conditions and products are summarized in Tables 1 and 2.

Decomposition of Iron(II) Acetate. In this approachm Fe(II) acetate ($Fe(OAc)_2$) is transferred into TOA, DOE, or DPE with OA and heated under a flux of nitrogen until reaction takes place. Evaporated compounds are trapped and prevented from dropping back. The concentration of OA has strong influence on the time interval until decomposition is visible. By applying a 3-fold surplus of oleic acid (12 mmol vs 4.0 mmol $Fe(OAc)_2$), the reaction is observed only after 2 h at 250 °C. The reaction time can be shortened by applying higher reaction temperatures. Those reaction conditions yield typically small (4 nm) nanocrystals with a narrow size distribution of 5% (Figure 1a), which are oxidized to magnetite or maghemite during the isolation. The high concentration of OA inhibits the reaction and the

(48) Hussein, G. A. M. *J. Anal. Appl. Pyrol.* **1996**, *37*, 111−149.
(49) Pal, B.; Sharon, M. *Thin Solid Films* **2000**, *379*, 83−88.
(50) Itoh, H.; Takeda, T.; Naka, S. *J. Mater. Sci.* **1986**, *21*, 3677−3680.
(51) Itoh, H.; Uemura, T.; Yamaguchi, H.; Naka, S. *J. Mater. Sci.* **1989**, *24*, 3549−3552.
(52) Langlet, M.; Labeau, M.; Bochu, B.; Joubert, J.-C. *IEEE Trans. Magn.* **1986**, *Mag-22*, 151−156.

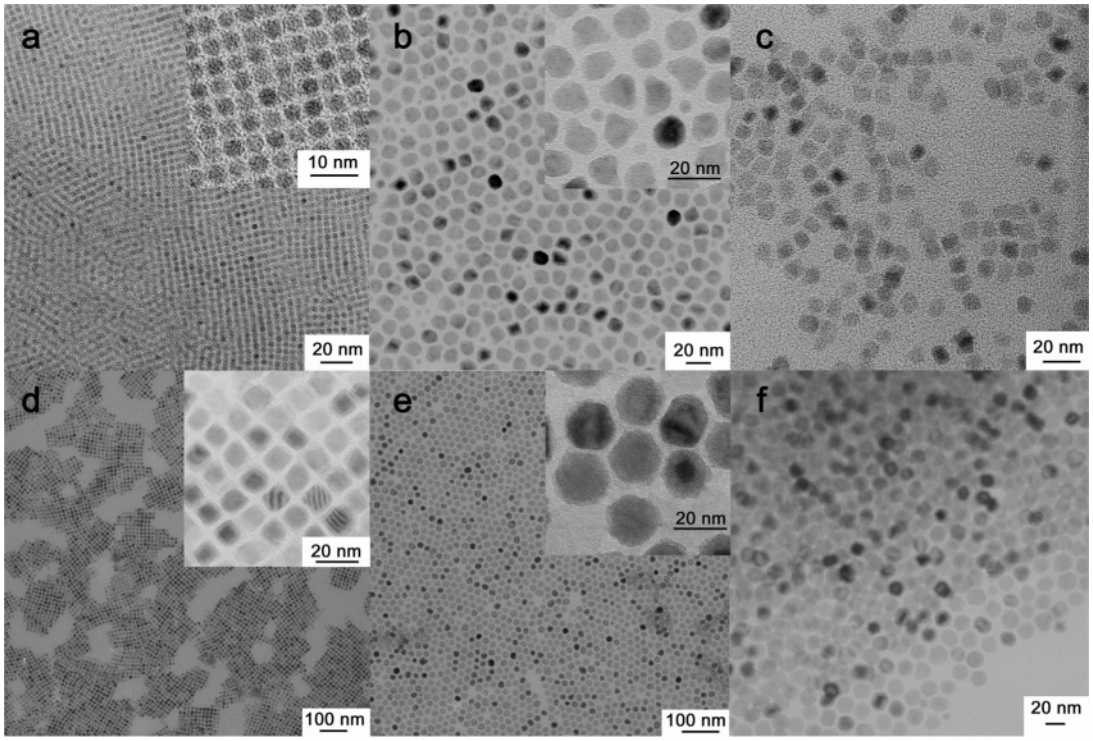

Figure 1. Nanocrystals obtained by decomposition of $Fe(OAc)_2$ in TOA at 250−260 °C. (a) 4 nm Fe_3O_4 or γ-Fe_2O_3 nanocrystals (4-fold surplus of OA, oxidized during isolation) forming superlattices. Inset: higher magnification of the image. (b) Irregular-shaped faceted particles of 14 nm and spherical particles of 5 nm obtained by decomposition of 8 mmol $Fe(OAc)_2$ in 12 mmol of OA/14 mL of TOA. (c) Cubic Fe_xO particle isolated in the early growth state (8 mmol of $Fe(OAc)_2$ vs 6 mmol of OA, 10 min at 255 °C). (d) Cubic Fe_xO nanoparticles isolated in a intermediate growth state (8 mmol of $Fe(OAc)_2$ vs 6 mmol of OA, 25 min at 255 °C). Inset: high-resolution TEM image of a bilayer of a simple cubic superlattice showing thickness fringes. (e) Large Fe_xO particles (mostly truncated octahedrons) isolated in a late growth state (8 mmol of $Fe(OAc)_2$ vs 6 mmol of OA, 80 min at 255 °C). Inset: high-resolution TEM image of the Fe_xO particles showing lattice fringes. (f) Large Fe_xO particles (mostly truncated octahedrons) isolated after stopping the reaction (8 mmol of $Fe(OAc)_2$ vs 6 mmol of OA, 140 min at 255 °C).

growth of the particles. At lower OA concentration (1.5 molar excess), it takes about 60 min at 250 °C. After a further 30 min, the reaction is stopped and all nanocrystals are precipitated with ethanol. A bimodal size distribution is observed (see Figure 1b). Large particles with various irregular shapes (long axis 14 nm, 8% SD) are mixed with small spherical particles (5 nm, 15% SD). The bimodal distribution can be separated by careful precipitation of hexane solutions with acetone, separating large particles from small particles. The best control over particle size, distribution, and uniformity is accomplished by further reducing the amount of oleic acid. Figure 1c−f shows particles evolving during the decomposition of 8 mmol of $Fe(OAc)_2$ dispersed in 6 mmol of OA and 14 mL of TOA. The decomposition is obvious within minutes after reaching 255 °C. TEM images of a sample taken after 10 min show small Fe_xO cubes with diagonal length of 12 nm (edge length of 8 nm, SD 8%). After an additional 15 min, the cubes have grown to a diagonal length of 15 nm (edge length of 11 nm, SD 7%, Figure 1d). The shapes are more regular compared with the smaller diameter samples, which facilitates the assembly into simple cubic superlattices, even during fast evaporation of the solvent. Additional reaction time leads to further growth of the particles. The particle shapes change to (mostly) truncated octahedrons (18 nm, SD 8%, Figure 1e), which are sometimes elongated in one direction. After 140 min at 255 °C the particle size increases, leading to particles that are more difficult to stabilize in solution due to increasing van der Waals forces (and possible magnetic dipole contributions). Aggregation makes the measurement of a representative value for the mean diameter from TEM images not as reliable, but the estimated average size is ∼19 nm (Figure 1f). The temperature and time dependence of the reaction can be attributed to the decomposition of different intermediates. In the case of a surplus of oleic acid, the formation and subsequent decomposition of iron(II) oleate is dominant; in the case of excess acetate, both species might contribute to the decomposition and also both anions might act as surfactant to control the growth rate and stabilization of the evolving nanoparticle.

Decomposition of Iron Pentacarbonyl and Subsequent Oxidation with PyO. For the decomposition of Fe(II) salts, we examined a tunable oxidation method applicable in organic solvents. Hyeon et al. have recently shown that iron nanocrystals can be oxidized to maghemite with trimethylamine *N*-oxide.[20] In this approach, either the iron nanocrystal is oxidized in a separate step or maghemite is directly synthesized by decomposition of iron pentacarbonyl in the presence of the oxidizer. We used similarly synthesized nanocrystals to assemble them in combination with PbSe nanocrystals into binary AB_2, AB_{13}, or AB_5 superlattice structures.[53]

During our investigations, we tested pyridine *N*-oxide (PyO). It is known that the oxidation potential of aromatic *N*-oxides is lowered in comparison with that of alkyl-substituted *N*-oxides and therefore may favor only partial oxidation to form, for example, Fe_3O_4.[54] When PyO is used to oxidize preformed iron nanocrystals (around 10 nm), aggregation is observed at high

(53) Redl, F. X.; Cho, K.-S.; Murray, C. B.; O'Brien, S. *Nature (London)* **2003**, *423*, 968−971.
(54) Ochiai, E. *Aromatic Amine Oxides*; Elsevier Publishing Co.: Amsterdam, 1967.

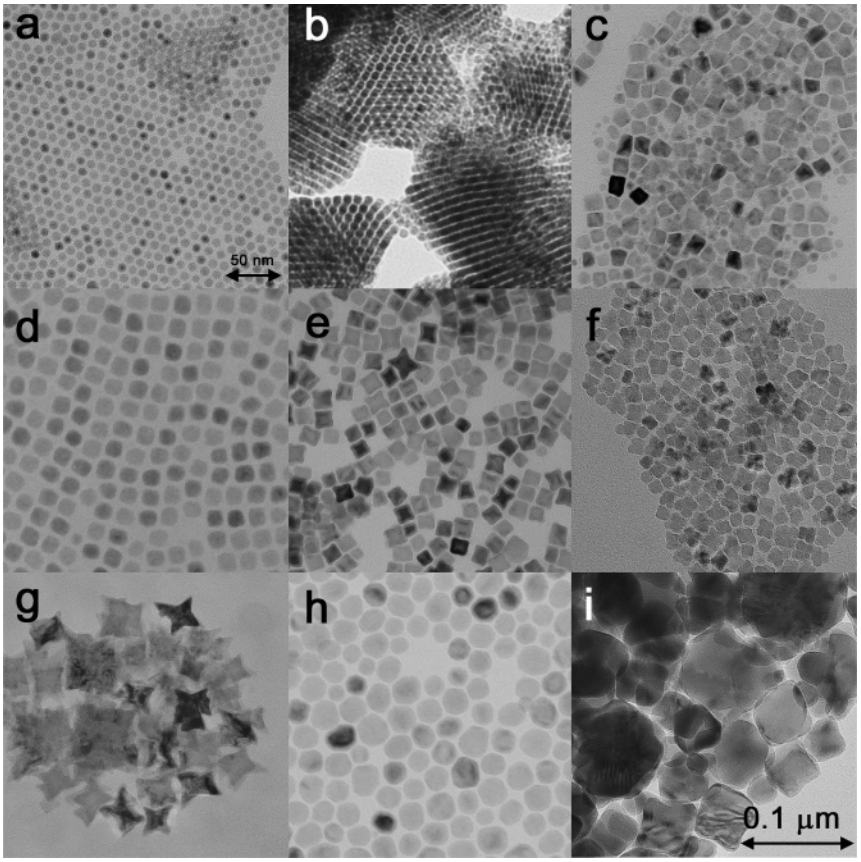

Figure 2. TEM images of nanoparticles produced by the decomposition of iron pentacarbonyl in DOE or TOA in the presence of LA and PyO. (a) Spherical particles of 8 nm size. (b) Superlattices of 8 nm nanoparticles. (c) Mixture of spherical and cubic particles, which have a diagonal length of roughly twice the diameter of the spherical particles. (d) Cubic particles of 13 nm edge length and 18 nm diagonal length. (e) Cubic and "star-shaped" particles. (f) Aggregates of spherical particles forming "cubic" particles. (g) Larger "star-shaped" particles. (h) Larger strongly faceted particles. (i) Large cubic particles composed of α-Fe and Fe_3O_4.

temperatures (>300 °C), resulting in large particles composed of α-Fe, magnetite, and wüstite. Under the same conditions, trimethylamine *N*-oxide yields uniform iron oxide (either γ-Fe_2O_3 or Fe_3O_4) of narrow size distribution and similar size compared with the starting material.

At lower temperatures (∼250 °C), the oxidation of iron particles with PyO yields magnetite or maghemite without aggregation. Despite peak-broadening, Bragg reflections match better with the reference values of magnetite. Nanocrystals have a broad size distribution and an average size smaller than the observed narrow size distribution (<10%) of the initial Fe nanoparticles. Because of the similarity of the high-temperature reaction products in the case of oxidation with PyO with the decomposition of $Fe(acac)_2$ (Supporting Information), it is assumed that the initial iron particles are oxidized to Fe_xO, which undergoes a subsequent reaction to iron and magnetite, accompanied by particle aggregation. The increased size of these large particles/aggregates inhibits complete oxidation by a surplus of pyridine *N*-oxide. Similar experiments at lower temperatures in DOE (in which the decomposition is no longer favored) have shown that the initial particles are small enough (6−8 nm) to allow a complete oxidation, consistent with observations of nanocrystal oxidation in air. This process is accompanied by a pronounced increase in size distribution and by the evolution of smaller particles with various shapes. We conclude that etching and recrystallization must be responsible for this size evolution.

The observed changes in oxidation profile due to PyO prompted a survey of the iron pentacarbonyl decomposition reaction in the presence of the PyO. Typically, pyridine *N*-oxide was added at 100 °C to a solution of LA in DOE, shortly followed by the iron pentacarbonyl. Within the first minutes after addition of the iron pentacarbonyl, the color of the solution changes to a dark red, indicating a reaction between the iron precursor and PyO. The absorption spectrum of the intermediate species is shown in Figure 6 in the Supporting Information. The mixture is kept at 120 °C for 1 h under nitrogen. Afterward the solution is heated (usually 10−20 °C/min) to the reaction temperature (typically the boiling point of the solution). DPE, DOE, and TOA were used as solvents. The boiling temperature of DPE is too low to achieve a sufficiently rapid decomposition rate; therefore, the particles exhibiting a broad size distribution can be isolated only after 2 h reaction time. In contrast, the higher boiling solvent TOA allows decomposition and formation of particles within 30 min, with accurate control over temperature (Figure 2c,g,h). Temperatures above 300 °C promote phase transition and aggregation (see Figure 2i) of the particles. The most reproducible results were obtained with DOE as solvent (see Figure 2a,b,d−f). The boiling point of 296 °C allows a sufficient reaction rate, whereas the temperature is low enough to largely avoid disproportionation and aggregation. Further experiments with similar concentrations of precursors proved that nanocrystals formed in DOE have a narrower size distribution (5−10%) and more regular shapes (cubic or spherical)

Scheme 2. Proposed Reaction Scheme with a Fast Preliminary Acid−Base Reaction and Dimerization, Which Keeps the Effective Concentration of Pyridine *N*-Oxide (PyO) Comparably Low and Approximately Constant

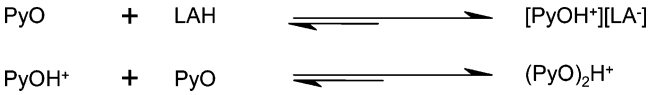

compared to those obtained in TOA. LA and OA were tested as surfactants. LA was found to be more advantageous because less polymeric side products were produced.

Table 2 lists the experiments and observations for the iron precursor decomposition reactions in the presence of PyO. The product of the reaction is mainly governed by temperature and solvent. In this context, the boiling point of the solvent (DOE) is a convenient limit to adjust the temperature. In addition, aggregation is less pronounced in DOE compared with TOA, under identical reaction conditions.

The concentration of surfactant was varied between zero and a 4-fold surplus with regard to the $Fe(CO)_5$. Without LA, iron pentacarbonyl reacts instantaneously with PyO dispersed in DOE at 100 °C, which is visible as a black oily precipitate and gas evolution, presumably due to decarbonylation similar to reactions of trimethylamine *N*-oxide with iron carbonyls.[55] In the presence of LA, gas evolution was noticed only at higher temperatures (in general between 170 and 200 °C). Pyridine starts to boil at ∼220 °C. In the case of a 4-fold surplus of LA vs PyO, no reaction was observable within a few hours. Our findings suggest the type of reaction mechanism depicted in Scheme 2, which is based on an equilibrium reducing the amount of effective (*free*) oxidizer in solution. PyO can react as a base with LA or form strong heteroconjugates with the acid. Further, dimerization of $PyOH^+$ and PyO also reduces the concentration of PyO in solution.[56,57] According to pK_a values of $PyOH^+$ in organic solvents and the heteroconjugation, the concentration of (*free*) PyO might be lowered noticeably in comparison to the concentration of iron pentacarbonyl.

In principle, the decomposition of iron pentacarbonyl can be promoted by LA, as well as pyridine, which evolves during the consumption of PyO. It is known that surfactants or reactants such as pyridine, *N*-methylpyrolidone, oximes, imines, or dienes accelerate the decarbonylation and final decomposition.[58] The initial step in these reactions is formulated as a disproportionation. The decarbonylation in pure solvent is inefficient, because of the predominant equilibrium between $Fe(CO)_5$, $Fe_2(CO)_9$, and CO. Furthermore, adsorption of CO on iron seeds inhibits catalytic growth and decomposition on the metal surface.

To determine whether disproportionation plays a role in the reaction, samples of the solution were characterized ex situ with IR spectroscopy (see Supporting Information Figure 5). LA dissolved in DOE shows typical absorptions of the CO stretch vibration of monomer and dimer in solution (dioctyl ether) at 1740 and 1712 cm^{-1}. After addition of PyO (which has only low solubility in DOE without the addition of LA) these absorptions become broader and a shift in the broad OH absorption of the acid is recognizable, indicating heteroconjugation or proton exchange between the acid and the base. After addition of $Fe(CO)_5$ and heating to 170 °C, the typical carbonyl absorption modes of the equatorial and axial ligands at 2020 and 2000 cm^{-1} are still recognizable, whereas the CH bending modes of the PyO are already reduced. After reaching higher temperatures (220 and 290 °C), the carbonyl stretching modes and CH bending modes of PyO have completely vanished. The results indicate the complete decarbonylation of the iron pentacarbonyl at temperatures higher than 170 °C under consumption of PyO. GC−MS data show that, in the course of the reaction, different alkyl-substituted pyridines (R−Py) evolve, which can be expected to contribute to the surface chemistry of the reaction. It seems likely that the initial decomposition of the iron pentacarbonyl is accompanied by the oxidation of the iron to Fe^{2+} and that the final reaction, yielding Fe_xO nanoparticles, is a decomposition of e.g. iron(II) laurate (similar to the decomposition of iron oleate or iron acetate reported in the previous paragraph).

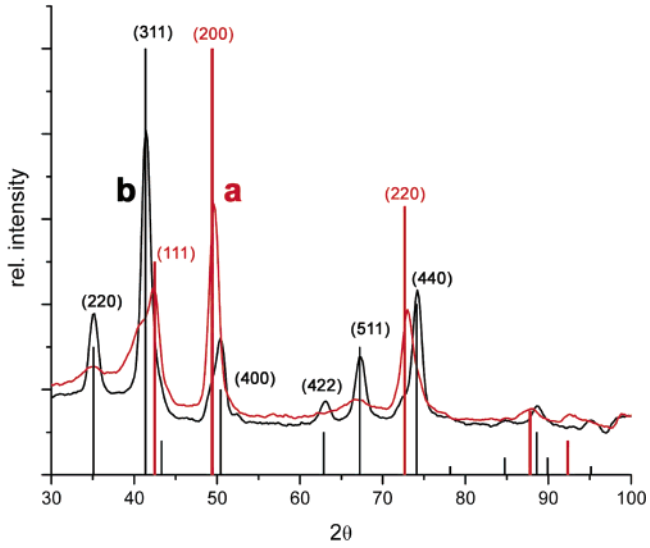

Figure 3. X-ray diffraction patterns from film-casted cubic wüstite nanocrystals of 12 nm edge length (a) before and (b) after annealing at 400 °C under nitrogen for 30 min.

Overall, it can be stated that the acid−base equilibrium has a strong influence on the reaction and the resulting product, and the correlation between concentration and particle size, shape, and size distribution is nontrivial. Particle size can be varied over a range of 8 nm (spheres) to ca. 17 nm (diagonal length of cubes) by changing the concentrations of all precursors simultaneously in DOE and by adjusting the reaction time. Distributions of diameter are typically below 10% RMS without size selection.

Structural Characterization. The iron oxide nanoparticles were characterized by X-ray diffraction, differential scanning calorimetry (DSC), electron diffraction, and bright-field and dark-field TEM techniques. Due to the sensitivity of the wüstite phase to oxygen, we have based our observations on a series of structurally identical wüstite samples over a composition range of 0.83−0.96.

As can be seen from Figure 3a, the observed Bragg reflections match well with Fe_xO reference values (JCPDS 01-1223). It is known that the lattice constant of nonstoichiometric Fe_xO depends on the amount of iron.[59] By utilizing this linear

(55) Burke, S. D., Danheiser, R. L., Eds. *Oxidizing and Reducing Agents*; John Wiley & Sons: New York, 1999.
(56) Chmurzynski, L. *Anal. Chim. Acta* **1996**, *321*, 237−244.
(57) Chmurzynski, L. *Anal. Chim. Acta* **1996**, *329*, 267−274.
(58) Smith, T. W.; Wychlck, D. *J. Phys. Chem.* **1980**, *84*, 1621−1629.
(59) McCammon, C. A.; Liu, L. *Phys. Chem. Miner.* **1984**, *10*, 106.

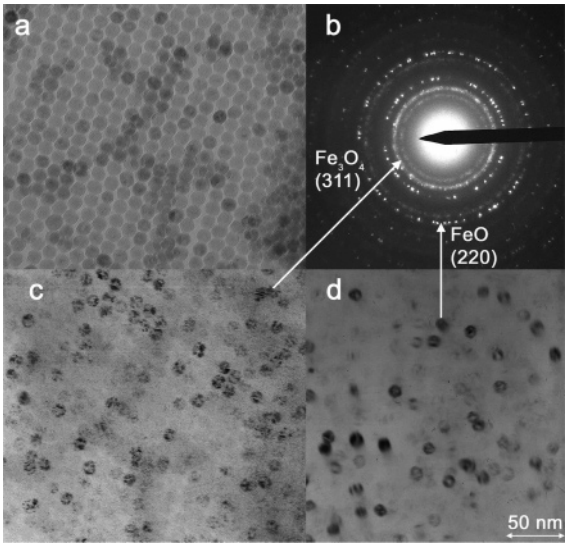

Figure 4. (a) TEM image of wüstite nanocrystals with seeds of magnetite inside. (b) SAED (selected area electron diffraction) of the specimen showing a speckled pattern for Fe_xO reflections and diffuse rings for magnetite reflctions. (c) Dark-field image of the region in panel a (shown as negative); a part of the magnetite reflections was selected with the objective aperture. (d) Dark-field image of the region in panel a (shown as negative); a part of the wüstite reflections was selected with the objective aperture.

relationship, one can calculate the iron content from X-ray diffraction patterns (see Tables 1 and 2). Applying this to our materials usually gives values within the validity range (0.83 to about 0.96) of the linear relationship. In general, smaller particles display a higher content of Fe^{3+}, which is probably due to the stronger influence of oxidation during isolation and measurement in air. The formation of nearly stoichiometric Fe_xO, which has been reported recently as a consequence of a two-step disproportionation of nonstoichiometric wüstite,[16,60] has not been observed. The first step is the formation of magnetite and nearly stoichiometric Fe_xO, which is reported to take place around 470 K. The final decomposition of the stoichiometric Fe_xO happens at temperatures higher than 530 K, indicating a higher stability of the stoichiometric Fe_xO under those nonequilibrium conditions.

Figure 4a shows the TEM image of self-assembled faceted Fe_xO nanocrystals. The SAED pattern (at high magnification) of those nanocrystals is typical for nearly all obtained Fe_xO nanocrystals. Usually there are two rings of spots belonging to the {200} and {220} reflections of wüstite and two broader rings with less intensity for larger *d* spacing, which belong to magnetite [(311) and (220)] with obviously smaller particle size. From X-ray diffraction (e.g., see shoulders in Figure 3a belonging to the maghemite phase), the magnetite crystallite size can be calculated to be smaller than 3 nm from line-broadening (Lorentz fits were applied to determine size from the (311) reflection according to the Debey−Scherrer equation). The most intense diffraction rings of both phases are well separated, enabling us to distinguish between the two phases by dark-field TEM imaging. Figure 4c shows the negative of the dark-field image of Figure 4a by selecting a fraction of the (311) reflection of magnetite. Figure 4d shows a part of the wüstite nanocrystals by selecting a fraction of the (220) reflection of wüstite. On the basis of the observation of diffuse rings in the SAED for magnetite, versus diffraction spots for magnetite, we conclude that the particles are mainly composed of the Fe_xO phase with small seeds of magnetite included. The seeds are about 2 nm in size (matching calculated particle sizes from line broadening in XRD) and show similar orientation within a single wüstite particle, concluded from the visibility of multiple seeds in single particles by choosing only a small part of the diffraction ring pattern. It is not surprising that the orientation of the arising magnetite is guided by the parent wüstite structure: both structures are based on fcc lattices of oxygen, whereby the first step of the proposed reaction of wüstite into magnetite and nearly stoichiometric wüstite can be thought of as diffusion of iron ions within the oxide framework.

Figure 3a shows an X-ray diffraction pattern typical for the obtained cubic or spherical Fe_xO particles (about 11−13 nm in size). In addition to the wüstite reflection, a shoulder at $2\theta = 41°$ is visible which we believe corresponds to the magnetite seeds within the wüstite particles. The wüstite particle size calculated from peak broadening is slightly less than the average size derived from TEM images (e.g., 11 nm spherical particle are calculated to be 8−9 nm in size from peak broadening). Annealing of the wüstite particles at 400 °C for 30 min converts the material nearly completely to magnetite and α-Fe, determined unequivocally from SAED during annealing of the sample on the heating stage of the TEM at 400 °C (see Supporting Information Figure 6). Heating to temperatures above 600 °C leads to the back-formation of wüstite. No change of particle size or shape can be observed during the transformation of the material; only changes in contrast of individual particles are obvious. During the decomposition, a lighter shell surrounding the particles is formed, which is most likely due to decomposition of surfactant and formation of a uniformly deposited surface carbon coat.[43] It is reported for large Fe_xO particles that the decomposition around 530 K forms complex particles composed of layers of α-Fe and magnetite, which are back-transformed to wüstite at temperatures over 833 K.[61,62]

X-ray powder diffraction analysis of the decomposition product at 400 °C shows in most cases only reflections for magnetite (see Figure 3a, measurement in air). The initially formed iron is oxidized during handling in air after the heat treatment. It seems likely that this is facilitated by a core−shell structure with iron on the outside of the particle. This core−shell structure can be explained on the basis of the observed Fe_xO structure incorporating small magnetite seeds, which function as seeds for further growth in the final reaction. This indicates a simultaneous process of diffusion of iron ions into tetrahedral sites and electron transfer combined with migration of excess iron away from the core, leading to growing magnetite cores encased by iron. The wüstite−α-Fe/magnetite phase transition was monitored by DSC with two consecutive runs (Supporting Information Figure 7) using the wüstite nanocrystals depicted in Figure 4a. The second run shows no transformation and is therefore taken as reference, dividing exothermic or endothermic heat flow. A very broad exothermic response with a maximum at 150 °C is due to the transformation of wüstite. The endothermic "melting" (order−disorder transition) of the surfactant is probably hidden by the decomposition. Features at 310 °C, 340 °C,

(60) Voncken, J. H. L.; Bakker, T.; Heerema, R. H. *Neues Jahrb. Mineral., Monatsh.* **1997**, 410−422.
(61) Tokumitsu, K.; Nasu, T. *Scr. Mater.* **2001**, *44*, 1421−1424.
(62) Tokumitsu, K.; Nasu, T. *Mater. Sci. Forum* **2000**, *343*−*346*, 562−567.

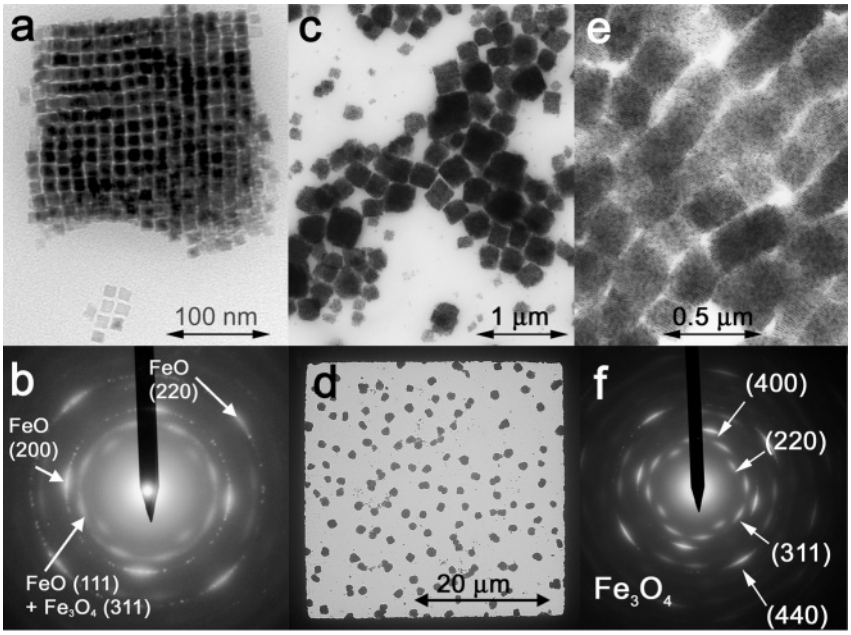

Figure 5. (a) TEM image of a single cubic superlattice built of cubic Fe_xO nanocrystals with 11 nm edge length. (b) SAED of the cubic superlattice showing strong reflections of the Fe_xO phase and weak reflections typical for magnetite. Orientational ordering is obvious from the inhomogeneous but symmetrical distribution of the reflections. (c) TEM image of an irregular gathering of cubic superlattices (0.1 μm up to about 0.5 μm). (d) Nearly exclusive formation of cubic superlattices homogeneously distributed over one 40 $\times$ 40 μm square of the TEM grid. (e) TEM image of rectangular and oriented superlattices obtain during the evaporation of solvent (hexane/octane) in a magnetic field parallel to the observed long axis of the superlattices. (f) SAED of an originally Fe_xO superlattice after disproportionation (and oxidation in air) to magnetite. The orientational ordering is preserved in the transformation to the higher oxidation state.

and higher temperatures can be attributed to the decomposition of excess oleic acid and surface-bound oleic acid.[63]

Particle sizes of magnetite obtained by annealing of wüstite films correspond well with the initial wüstite particle size. The phase transition happens, therefore, without aggregation and particle growth. The wüstite nanocrystals can be directly converted to maghemite, γ-Fe_2O_3, by annealing in oxygen at 200 °C for 1 h. Even if the structures of maghemite and magnetite are very similar, both phases obtained from the same cubic nanocrystals can be clearly identified and distinguished. Both match perfectly with the corresponding reference values. According to this, it is possible to obtain cubic nanocrystals of magnetite and maghemite of about 11−13 nm, which is usually cannnot be accomplished by direct synthesis.

Self-Assembly of Iron Oxide Nanocrystals into Superlattices. The selective oxidation synthesis of wüstite allows reproducible generation of spherical nanocrystals of 8−10 nm in size or cubic nanocrystals between 11 and 13 nm in size (edge length). The highly narrow size distribution (diameters with 5−10% rms) of the particles facilitates their assembly in long-range ordered superlattices. The spherical and sometimes faceted particles form the most densely packed superlattices (Figures 2b and 4a) with sharp edges and hexagonal shape.[64]

Superlattices built from cubic Fe_xO nanocrystals are shown in Figure 5. The particles assemble effectively despite fast solvent evaporation rates. In the limit of spatially homogeneous evaporation, where the boundaries of nanoparticle domains remain fluxional throughout the growth dynamics, the evaporation rate is not believed to be an important parameter.[65] The particles arrange nearly exclusively into cubic superlattices (Figure 5a,c,d) which are visible under an optical microscope (Figure 6a, a superlattice of superlattices). Interestingly, most of those cubic superlattices have similar sizes (around 200 nm, which corresponds to a two-dimensional array of 17 $\times$ 17 cubes). This indicates a widespread homogeneous and simul-

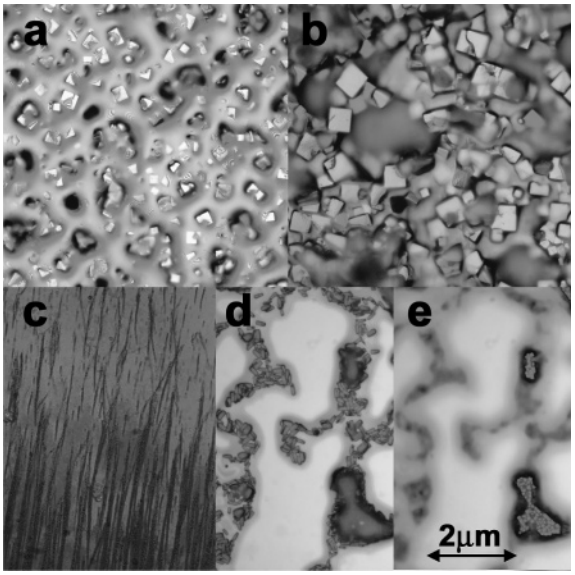

Figure 6. Optical microscope images of self-assembled superlattices of cubic wüstite nanocrystals. (a) Material as obtained from syntheses. (b) After annealing of a deposited film on a glas substrate at 200 °C in 5% forming gas. (c) Needles of aggregated superlattices aligned during deposition by an external magnetic field parallel to the surface. (d) Rectangular superlattices formed during self-assembly of cubic nanocrystals in a magnetic field perpendicular to the substrate. (e) Same region as in panel d with focus stepped up in the *z*-direction, showing assemblies of pillars of superlattices pointing toward the observer in the direction of the applied external magnetic field.

(63) Osman, M. A.; Suter, U. W. *Chem. Mater.* **2002**, *14*, 4408−4415.
(64) Collier, C. P.; Vossmeyer, T.; Heath, J. R. *Annu. Rev. Phys. Chem.* **1998**, *49*, 371−404.
(65) Rabani, E.; Reichman, D. R.; Geissler, P. L.; Brus, L. E. *Nature* **2003**, *426*, 271−274.

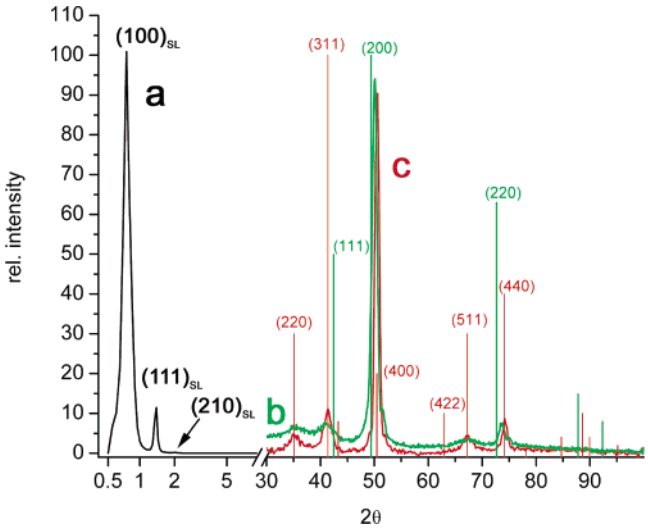

Figure 7. X-ray diffraction analysis of solution casted films on a Si substrate. (a) Small-angle Bragg reflections from the cubic superlattice. (b) Wide-angle diffraction pattern. (c) Wide-angle diffraction pattern after annealing at 200 °C in 5% H_2/Ar.

taneous nucleation event during the solvent evaporation. These superlattices are stable under annealing conditions (Figure 6b), whereby the single particle sizes remain unchanged, as proven by line broadening in X-ray diffraction. As discussed in the Structural Characterization section (above), the crystals are terminated by {100} surfaces. The high symmetry of the crystal lattice and the supposedly preferable plane-to-plane arrangement of the nanocrystal lead to orientational ordering in superlattices, as confirmed by SAED and small-angle and wide-angle X-ray diffraction. The SAEDs in Figure 5b,f were recorded from single cubic superlattices of Fe_xO before and after decomposition. The uneven but symmetrical distribution of the {220} and {200} Fe_xO or (220), (311), (400), and (440) Fe_3O_4 Bragg reflections clearly indicates identical orientation of the crystallites. The reflections in the small-angle X-ray diffraction pattern (Figure 7a) can be identified as $\{100\}_{SL}$ (plane spacing of 13.6 nm) and $\{111\}_{SL}$ (plane spacing of 7.5 nm), corresponding to a simple cubic arrangement of the subunits, which maximizes particle interaction by shared interfaces. The calculated crystal dimension of 13.6 nm matches the dimension of the crystal size (11 nm) and the additional spacing (2 nm) governed by interdigitating oleic acid molecules on the particle surface.

The alternate arrangement that might also fit the data, the fcc superlattice (Supporting Information Scheme 1), can be ruled out by SAX results and TEM observations. Because there is no free space in this arrangement, a high particle density of about 0.84 is reached, exceeding the density of fcc or hexagonal close-packed (hcp) ordered spheres. The wide-angle X-ray diffraction pattern of self-assembled cubic superlattices of Fe_xO nanocrystals in Figure 7b displays an intensity distribution which is clearly different from the values expected for a random orientation of crystallites. This can be explained as resulting from cubes of Fe_xO lying with {100} surfaces on the substrate. The three degrees of rotational freedom are reduced to two. The highest reflection intensity is therefore found for the (200) plane, which is parallel to the surface (*z*-axis defined perpendicular to the substrate). Similar to this consideration, SAED should give the highest intensities for (200), (020), or (220) reflections (see Figure 5b). The superlattices are stable under annealing conditions. The superlattices were annealed in a reducing atmosphere (5% forming gas) at 200 °C for 30 min (which is insufficient to reduce the iron oxides), leading to the decomposition of the wüstite into magnetite and iron, which is oxidized before the X-ray diffraction measurement during handling in air. The resulting X-ray pattern in Figure 7c again shows an intensity distribution not typical for isotropic distributed crystallites. The crystal structure of the resulting magnetite is based on the fcc oxygen substructure in the parent Fe_xO phase. Similar to Fe_xO, the highest intensity reflection originates from the (400) plane parallel to the surface plane and therefore parallel to the substrate plane.

Self-assembly of the cubic nanocrystals can be directed by an external magnetic field. Figure 5e shows a TEM image of superlattices formed in a weak external magnetic field (two small permanent magnets) parallel to the grid surface. The superlattices are aligned in the direction of the magnetic film and form needle-like structures by a sequence of neighboring superlattices. It is interesting to note that most superlattices have a rectangular shape, with the long axis parallel and the short axis perpendicular to the external field, presumably maximizing constructive interparticle forces, whereas superlattices deposited under zero field are of square shape and randomly oriented. The nanocrystals are observed to align according to a combination of the evaporation-driven self-assembly and the influence of the magnetic field. This phenomenon can also be observed under the light microscope. Figure 6c shows needles of superlattices up to a few micrometers long, which are formed under a parallel magnetic field. If the external magnetic field is perpendicular to the substrate, shorter-range superlattices are formed, either lying flat on the surface or building bundles of pillars in the direction of magnetic field (see Figure 6d,f).

Since the assembly process is influenced by an external magnetic field, we conclude that the nanoparticles are behaving either like free paramagnetic spins (wüstite) or like superparamagnetic particles (coupling of spins that would be expected in magnetite seeds in the particles). The weak magnetic response of the cubes is crucial, because on one hand it allows the alignment by an external magnetic field and on the other hand magnetic dipole attraction between the particles at room temperature is low, which promotes this type of hierarchical self-assembly.

Mössbauer Characterization. Structural characterization gave a clear indication of the simultaneous existence of both wüstite and magnetite phases in the nanocrystals, with the propensity of conversion to the more oxidized state. Mössbauer spectroscopy was performed in order to gain full insight into the behavior and relative compositions of Fe^{2+} and Fe^{3+} in the different oxygen coordination environments. Mössbauer studies[66] were conducted on four samples: First, the original, as-prepared sample of Fe_xO/Fe_3O_4 cubic nanocrystals (sample 1) was prepared according to the procedure described previously, with further detail in Table 3. Sample 1 was then calcined in nitrogen at 200, 400, and 600 °C for 5 min, to give samples 2, 3, and 4, respectively (see Table 3). Data were collected at sample temperatures in the range 4.2 K < T < 300 K. The spectra exhibited complex magnetic interactions due to the presence of multiple magnetic phases within a particle and

(66) Greenwood, N. N.; Gibb, T. C. *Mössbauer Spectroscopy*; Chapman and Hall: London, 1971.

Table 3. Weighted Content of Various Iron Oxide Phases from Mössbauer Spectral fits at $T = 300$ K and Associated Blocking Temperatures, XRD, and TEM data

sample	Fe_xO (%)	Fe_3O_4 (%)	XRD, TEM	T_B (K)
1	51 (paramagnetic)	49 (superparamagnetic/interfacial)	7 nm Fe_xO, 3 nm Fe_3O_4	175
2	41 (paramagnetic)	59 (superparamagnetic/interfacial)	7 nm Fe_xO, 4 nm Fe_3O_4	138
3	7 (paramagnetic)	93 (intermediate relaxation)	10−12 nm Fe_3O_4	180
4	6 (paramagnetic)	67 (superparamagnetic and interfacial) 27 (magnetic)	18 nm Fe_3O_4, 6−7 nm Fe_xO	190

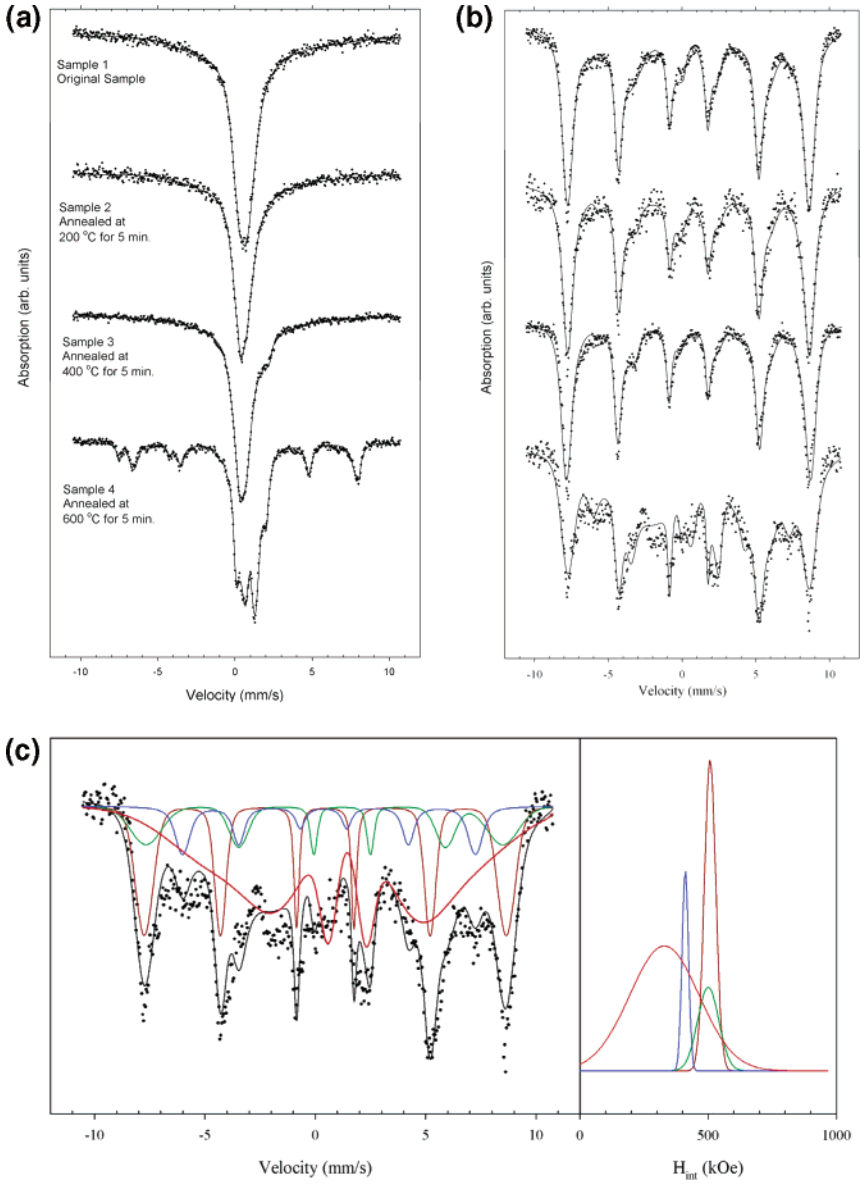

Figure 8. (a) Mössbauer spectra of samples 1−4 at room temperature. The solid lines are least-squares fits of the experimental points to the superposition of various iron-oxide phase. (b) Mössbauer spectra of samples 1−4 (from top to bottom) at 4.2 K. (c) Mössbauer spectra of sample 4 at 4.2 K. Individual component spectra in color depict contributions to the spectrum by various iron oxide phases. The solid line through the experimental points gives the least-squares fit of the experimental data to the resultant, convoluted theoretical spectrum. On the right, the internal magnetic field distributions for each subcomponent spectrum is given. Spectral components in brown and green are associated with the Fe^{3+} and Fe^{2+} sites of magnetite, respectively. The spectral component in blue is associated with crystalline, antiferromagnetic Fe_xO, and the broad component in red is associated with an interfacial Fe_xO/Fe_2O_4 amorphous, spin-glass-like phase.

superparamagnetic behavior typical of small, magnetically ordered particles.[67] Spectral fits were obtained assuming the superposition of spectral signatures due to (1) paramagnetic Fe_xO, (2) superparamagnetic Fe_3O_4, (3) magnetic Fe_3O_4, (4) antiferromagnetic Fe_xO, and (5) interfacial Fe_xO/Fe_3O_4 phases in various amounts, depending on sample calcination conditions and temperature of measurement.

Room-temperature Mössbauer spectra of the original and annealed samples are shown in Figure 8a. The solid lines are theoretical fits to the data assuming a superposition of spectral signatures corresponding to four distinct phases: (1) paramagnetic Fe_xO, simulated with a broad collapsed absorption line

(67) Dorman, J. L., Fiorani, D., Eds. *Magnetic Properties of Fine Particles*; Elsevier: Amsterdam, 1992.

Table 4. Weighted Content of Various Oxide Phases from Mössbauer Spectral Fits at $T = 4.2$ K

sample	Fe_xO (%)	Fe_3O_4 (%)	glass phase (%)
1	4	65	31
2	3	77	20
3	3	87	6
4	8	35	57
av H_{int} (kOe)	Fe^{2+}, 410	Fe^{3+}, 507 Fe^{2+}, 495	Fe^{2+}, 319

with isomer shift, $\delta = 0.88$ mm/s;[66] (2,3) superparamagnetic Fe_3O_4[68] and/or interfacial Fe_xO/Fe_3O_4, which are hard to distinguish; and (4) magnetic Fe_3O_4 phases.[66] Relative contributions of the various phases to spectral absorption areas are tabulated in Table 3. The results are in general agreement with TEM and XRD data interpretation, also included in Table 3. Percent areas can be translated to percent content of the various oxide phases, assuming similar Mössbauer efficiency (recoil-free fraction) for all phases.

With increasing annealing temperature, the percentage contribution of magnetite increases. The spectra of samples 1 and 2 are dominated by paramagnetic Fe_xO and superparamagnetic Fe_3O_4, giving a collapsed, featureless absorption line. At this expanded velocity range, the small quadrupole splittings associated with Fe_xO ($\sim$0.5 and 0.78 mm/s[66]) are not resolved. Spectra of sample 3 show the onset of intermediate magnetic relaxation effects, as the percentage of magnetite in the particles increases. Finally, sample 4, obtained at the highest calcination temperature used of 600 °C, contains large enough particles of magnetite (of an average diameter of 18 nm according to TEM measurements) to exhibit magnetic order at room temperature for the larger particles in the particle size distribution. In addition to superparamagnetic magnetite, the broad, collapsed central absorption area may contain contributions from Fe_xO inclusions and interfacial iron exhibiting intermediate relaxation effects.

With decreasing temperature the frequency of spin fluctuations, due to thermal activation, is decreased to a spin relaxation time longer than the characteristic measuring time for the Mössbauer technique, $\tau_{Möss} = 10^{-8}$ s. This causes the spectra to pass gradually from the collapsed superparamagnetic spectrum observed at room temperature to a magnetically split spectrum below 100 K (Supporting Information Figure 8a−d). The process is governed by a spin relaxation time $\tau = \tau_0 \exp(K_{eff}V/k_BT)$, for uniaxial magnetic anisotropy,[69,70] where K_{eff} is the effective magnetic anisotropy density, V is the volume of the particle, T is the temperature, k_B is Boltzmann's constant, and τ_0 is a constant characteristic of the material. The Mössbauer blocking temperature,[71] defined as the temperature where 50% of the total spectral absorption area is due to six-lined magnetic spectra, varied from $T_B = 138$ K for sample 2 to $T_B = 190$ K for sample 4 (Table 4), due to variations in average particle size, composition, and surface characteristics of the particles.

The blocking temperature is an effective measurement of the superparamagnetic energy barrier, which is given by the product of $K_{eff}V$. With higher calcination temperatures one observes larger average particle sizes due to sintering, and thus, higher blocking temperatures. This trend is generally observed in Table 4, with the exception of sample 2 as compared to sample 1. These two samples have the same average particle size of $\sim$7 nm diameter and fairly similar composition, and yet they exhibit different blocking temperatures. This is attributed to different surface characteristics of the particles. The as-prepared sample 1 consisted of particles coated with oleic acid, while the annealed particles have a carbon coating, due to the transformation of the surfactant upon annealing. It is well known that, in small magnetic particles, surface and strain contributions to K_{eff} dominate, producing magnetic anisotropy densities 2 orders of magnitude higher than the magnetocrystalline anisotropy of the corresponding bulk material.[72] Mössbauer blocking temperatures of nanoparticulate magnetite have been observed to be very sensitive to the exact nature of the surfactant or coating at the particle surface.[68]

In the bulk, Fe_xO undergoes a first-order magnetic phase transition from a paramagnetic to an anti-ferromagnetic state at $\sim$198 K. Magnetic features superimposed on the superparamagnetic envelope appeared in the Mössbauer spectra of the as-prepared sample 1 below 200 K marking this magnetic phase transition, as also observed in SQUID measurements. Superparamagnetism dominated the magnetic behavior of all four samples down to about 100 K. Detailed analysis of the superparamagnetic processes, collective magnetic excitations[73] below T_B, saturation magnetizations, and saturation internal hyperfine magnetic fields observed will be presented in future work.

Figure 8b compares the Mössbauer spectra obtained for the four samples at $T = 4.2$ K. Relatively sharp magnetic spectra are observed. For sample 4, however, the magnetic structure is superimposed on a broad, featureless absorption envelope. This envelope cannot be attributed to superparamagnetic processes, as at this temperature, far below the blocking temperature of the sample, spin fluctuations are completely frozen relative to the characteristic measuring time of the Mössbauer technique. The broad envelope is attributed to the presence of a spin-glass-like, amorphous, Fe_xO/Fe_3O_4 interfacial phase, as described below. The solid lines over the experimental data points in Figure 8b are the result of the superposition of four magnetic subspectra associated with the Fe^{3+} and Fe^{2+} sites of the spinel structure of ferrimagnetic Fe_3O_4, with Fe^{2+} sites of crystalline, antiferromagnetic Fe_xO and a glassy interfacial Fe_xO/Fe_3O_4 phase (see caption of Figure 8c for color-coded contributions of the various phases). The relative amounts of these phases derived from spectral absorption areas, by assuming similar recoil-free fractions for all phases, are tabulated in Table 4. This crucial assumption of equal recoil-free fractions, which is needed in order to translate Mössbauer spectral information to relative contents of the various phases, is more reliable at 4.2 K than at room temperature (300 K), because thermally activated lattice vibrations are hindered at low temperature.

In Figure 8c we present again the 4.2 K Mössbauer spectrum of sample 4. Above the experimental spectra, we present color-coded Mössbauer signatures of individual subcomponent contributions. To the right, color-coded magnetic hyperfine field distributions associated with each spectral signature are shown. Spectral components in brown and green are associated with the Fe^{3+} and Fe^{2+} sites of magnetite, respectively. The spectral

(68) Mørup, S.; Topsøe, H.; Lipka, J. *J. Phys.* **1976**, *37*, C6.
(69) Brown, W. F., Jr. *Phys. Rev.* **1963**, *130*, 1677.
(70) Brown, W. F., Jr. *J. Appl. Phys.* **1968**, *39*, 993.
(71) Papaefthymiou, G. C. *MRS Proc.* **1994**, *332*, 195.
(72) Papaefthymiou, G. C. *MRS Proc.* **2000**, *395*, C2.4.1 and references therein.
(73) Mørup, S.; Topsøe, H. *Appl. Phys.* **1976**, *11*, 63.

Table 5. Magnetic Data Correlated with X-ray Data

used particles (TEM)	$T_{annealing}$,[a] time	phase (crystal size[b])	H_{ex}/kOe (cooling field/kOe)	H_c/kOe (T)	M_s[c]/emu g^{-1} (at field/kOe)	features
mostly cubic NCs with a diagonal length of 14 nm and 12% SD						
1		Fe_xO (9 nm) Fe_3O_4 (3 nm)	1.75 (50)	2.00 (10 K)	48 (50)	FC (50 Oe): maximum at 200 K (T_N)
2	200 °C, 5 min	Fe_xO (10 nm) Fe_3O_4 (6 nm)	0.20 (50)	0.80 (10 K)	75 (70)	ZFC (50 Oe): max. at 200 K (T_N), FC (50 Oe): broad max. at 120 K
3	400 °C, 5 min	Fe_3O_4 (11 nm) α-Fe (40 nm)	0 (50)	0.97 (10 K)	76 (70)	ZFC and FC (50 Oe): decrease in magnetization between 120 and 100 K (Verwey transition)
4	600 °C, 5 min	Fe_3O_4 (14 nm) Fe_xO (7 nm)	0 (50)	1.3 (10 K)	77 (70)	ZFC and FC (50 Oe): decrease in magnetization between 120 and 100 K (Verwey transition)
cubic NCs with a diagonal length of 12 nm and 8% SD						
	as synthesized	Fe_xO (10 nm) Fe_3O_4	1.50 (10)	0.28 (5 K)	7 (10)	FC (50 Oe): maximum at 200 K (T_N)
	after 4 weeks at RT under nitrogen		2.13 (20)	2.60 (5 K)	27 (50)	
	150 °C		0.45 (10)	1.00 (10 K)	30 (20)	
	350 °C, 4 min		0.1 (10)	0.63 (10 K)	45 (20)	ZFC and FC (50 Oe): T_b at 270 K and increase in magnetization between 125 and 90 K (T_N)
	250 °C, 1 h, in air		0 (10)	0.17 (5 K)		particles are oxidized to maghemite, T_b > 300 °C, broad max. in ZFC, FC

[a] All samples are annealed in a nitrogen atmosphere unless otherwise noted. [b] Calculated from line broadening in X-ray diffraction powder pattern. [c] Not corrected for extraneous organic.

component in blue is associated with crystalline, antiferromagnetic Fe_xO,[74] and the severely broadened component in red is associated with an interfacial Fe_xO/Fe_2O_4 amorphous phase. The very broad distribution in the magnitudes of internal magnetic fields of the interfacial component indicates the presence of a frustrated spin system, due to competing ferromagnetic and antiferromagnetic interactions, producing a spin-glass-like phase.

The detailed characteristics of the glassy phase may depend on the length of annealing time, cooling rate, and other experimental conditions. For this sample, annealed at 600 °C for only 5 min in order to avoid excessive particle-size growth, the glassy component dominates, contributing about half of the total absorption intensity. The calcination temperature of 600 °C is higher than 570 °C, above which Fe_xO is stable. Thus, magnetite is expected to be transformed to wüstite at this temperature, in agreement with our conclusions in Table 4, which indicate a much larger sum for the percent contributions of Fe_xO and spin-glass phase in sample 4, as compared to the other three samples.

Magnetic Characterization. The magnetic properties of the iron oxide nanocrystals were studied together with their corresponding annealed products. The results are summarized in Table 5. Figure 9 displays ZFC and FC curves and hystereses loops obtained from cubic 12 nm wüstite particles with a size distribution of 8%. The ZFC of the as-synthesized material has a maximum at 220 K, the FC at 205 K. These maxima appear to mark the transition from paramagnetism to antiferromagnetism of wüstite, and correspond well with reported values. This transition is also recognizable in the temperature dependence of coercivity: zero at 220 K and 80 Oe at 200 K, reaching hyperbolically 285 Oe at 5 K (see Supporting Information Figure 9). The steady increase in coercivity of the wüstite particles with decreasing temperature might be due to the pinning of uncompensated surface spins, nonstoichiometry, or exchange coupling of the Fe_xO with incorporated seeds of magnetite in the initial material.[75] Figure 9b was obtained after the wüstite nanocrystals were annealed at 400 °C under nitrogen for 60 min. The heat treatment transfers the wüstite into a magnetite−α-Fe composite, while the iron is oxidized during the following transfer into the SQUID. ZFC and FC show a maximum at about 270 K for the transition from ferrimagnetism to superparamagnetism. Two further kinks with inflection points at 120 K in the ZFC and FC (see Figure 9b,j) could be attributed to the Verwey transition. Despite the clear appearance of the transition in ZFC and FC, the coercivity (Supporting Information Figures 9 and 10) is steadily increasing and does not display the reported local minimum[76] around the transition, which is assumed to be due to shape anisotropy. The Verwey transition causes some remarkable changes in properties, e.g., conductivity, magnetic moment, or specific heat, and is directly related to the presence of magnetite in these materials.[77] The highest temperatures (around 120 K) are obtained with synthetic magnetite under involvement of sophisticated syntheses and crystallization techniques, whereas the predicted influence of deviation from the ideal stoichiometry seems to be less important in small crystals between 30 and 50 nm.[78]

After oxidation of the cubic particles at 200 °C in oxygen ZFC and FC curves, the magnetization increases toward a broad maximum close to room temperature, exceeding our available measurement range. The annealing conditions do not lead to crystal growth but remove surfactant very efficiently. The reduced spacing between the maghemite cubes allows stronger magnetic dipole coupling, leading to a broad maximum shifted to higher temperature.[79,80] These measurements demonstrate how wüstite crystals can be used to generate different magnetic materials with distinct properties. The hystereses loops in Figure

(74) Shechter, H.; Hillman, P.; Ron, M. *J. Appl. Phys.* **1966**, *37*, 3043.

(75) Dimitrov, D. V.; Hadjipanayis, G. C.; Papaefthymiou, V.; Simopoulos, A. *IEEE Trans. Magn.* **1997**, *33*, 4363−4366.
(76) Zhou, Z.-J.; Yan, J.-J. *J. Magn. Magn. Mater.* **1992**, *115*, 87−98.
(77) Walz, F. *J. Phys. Cond. Matter* **2002**, *14*, R285−R340.
(78) Guigue-Millot, N.; Keller, N.; Perriat, P. *Phys. Rev. B* **2001**, *64*, 012402/012401−012402/012404.

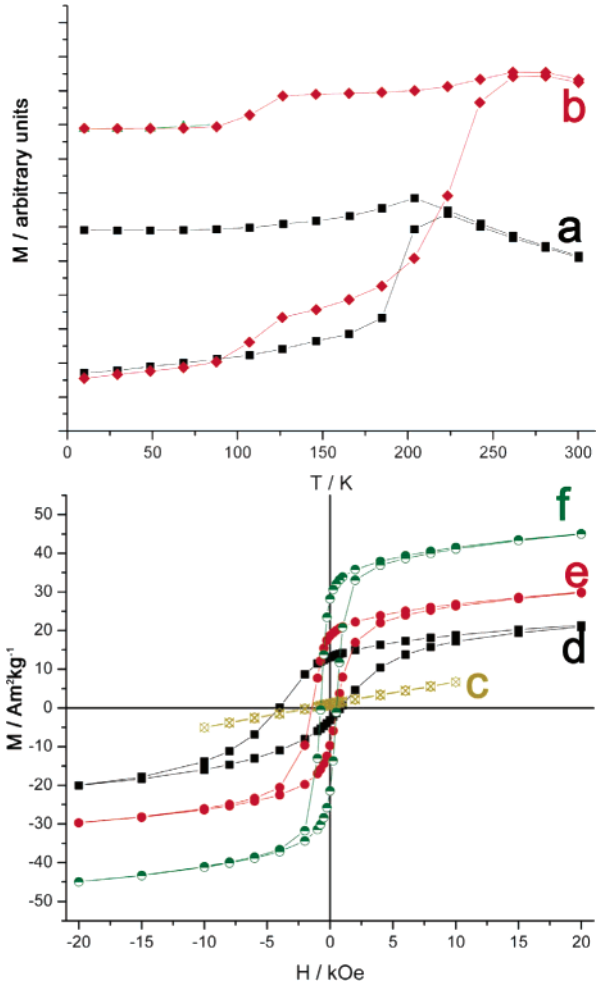

Figure 9. SQUID measurements of cubic Fe_xO nanocrystals with increasing amount of incorporated magnetite. ZFC and FC (both cooled at 50 Oe) of (a) as-synthesized nanocrystals (signal is scaled up by 1 order of magnitude (compared with b); (b) after annealing at 400 °C under nitrogen for 60 min. Hystereses loops of (c) the originally obtained material. Hystereses loops after field cooling of (d) the original material after storage for 4 weeks under nitrogen at room temperature; (e) after annealing at 150 °C under nitrogen for 30 min; (f) after annealing at 350 °C for 4 min. (No correction for the weight of the organic surfactant was applied. From elemental analysis the organic can be estimated to contribute about 30 wt %. Films were produced by evaporation of solvent on a Si substrate.)

9c−f show the magnetic response of material obtained by a stepwise thermally induced transition from wüstite to magnetite. Graph c shows the nearly linear response of the initially generated wüstite to the external magnetic field at 5 K. The linear response is typical for randomly oriented antiferromagnetic particles, the magnetic moments of which are pulled away from the ideal orientation by the external magnetic field, therefore leading to low magnetization.

The magnetic properties changed dramatically after the sample was stored for 4 weeks under nitrogen and at room temperature (Figure 9d). The magnetization (remnant and saturation) has increased multifold. After field cooling, a shift toward the opposite field is observed (H_{ex} = 2.1 kOe after field cooling at 20 kOe). Annealing at higher temperatures (Figure 9f, 150 °C for 30 min; Figure 9g, 400 °C for 4 min) leads to an increase in remnant and saturation magnetization, while the coercivity and the shift are reduced (although the absolute magnetization values presented are not corrected for extra organic and therefore are noticeabley reduced in comparison with bulk). These observations can be explained with the transition from wüstite to magnetite and iron. Interfaces between growing magnetite seeds in the wüstite matrix lead to exchange coupling between the anti-ferromagnetic wüstite and the magnetite, which leads to increased coercivity and a reduced remnant and saturation magnetization. SQUID measurements provide a means to follow the disproportionation of the wüstite nanocrystals accurately. The measurements have shown that controlled annealing can be used to engineer material with distinct magnetic properties ranging from anti-ferromagnetism to the magnetic moment of magnetite.

Electronic Conduction in Iron-Based Nanocrystal Devices. Electronic conduction in magnetic nanocrystal arrays is influenced by both the electrostatic energy for charging individual grains and the relative orientation of nanocrystal magnetic moments.[33−35,81] Previous devices formed from monolayers or multilayers of superparamagnetic hcp cobalt displayed negative magnetoresistance at low temperatures (i.e., increased conductivity as the individual nanocrystal magnetizations were aligned by an external magnetic field). Granular magnetite films[78,82] or sandwiched magnetite nanocrystals[33,81] have also been studied because of their half metallic properties and the metal−insulator transition at the Verwey temperature. The complex nature of the nanocrystals in this investigation makes them interesting candidates for similar types of studies. As described above, adjustment of nanoparticle composition is facilitated through temperature- and time-dependent decomposition and therefore allows simultaneous control over both the amount of conducting material (iron and magnetite) and the magnetic properties.

The two-terminal nanocrystal devices used in this study were constructed using a new technique which combines nanocrystal self-assembly with conventional microfabrication. Previous nanocrystal devices utilized self-assembly to close a 100 nm gap between gold electrodes[34,35] or utilized the Langmuir−Schäfer technique to form multilayers sandwiched between a conducting substrate and a top electrode.[33,81] In this case, device fabrication begins by using optical lithography and reactive ion etching to create holes of different sizes in an insulating SiO_2 layer deposited on a conducting Pt film. The device processing is depicted in Figure 10a. In the final device structure, the Pt layer comprises a bottom electrode while the SiO_2 film defines the lateral device area (see the optical microscope image of the wafer at this stage of fabrication in Figure 9a in the Supporting Information) and shows a series of different shaped holes of different sizes. The exposed Pt counter electrode appears light colored in the image.

Nanocrystal multilayers were self-assembled onto the patterned wafer (see Figures 9b in the Supporting Information) and annealed in a vacuum (450 °C, 1 h at 10^{-7} bar) prior to an in situ electron-beam evaporation of an Al top electrode. Devices were completed with a second lithography step and a wet-chemical etch of the Al to provide device isolation. A schematic cross section of the completed device is depicted in Figure 10b.

(79) Dai, J.; Wang, J.-Q.; Sangregorio, C.; Fang, J.; Carpenter, E.; Tang, J. *J. Appl. Phys.* **2000**, *87*, 7397−7399.
(80) Zeng, H.; Sun, S.; Vedantam, T. S.; Liu, J. P.; Dai, Z.-R.; Wang, Z.-L. *Appl. Phys. Lett.* **2002**, *80*, 2583−2585.
(81) Markovich, G.; Fried, T.; Poddar, P.; Sharoni, A.; Katz, D.; Wizansky, T.; Millo, O. *MRS Proc.* **2003**, *746*, Q4.1.
(82) Tang, J.; Kai-Ying; Zhou, W. *J. Appl. Phys.* **2001**, *89*, 7690−7692.

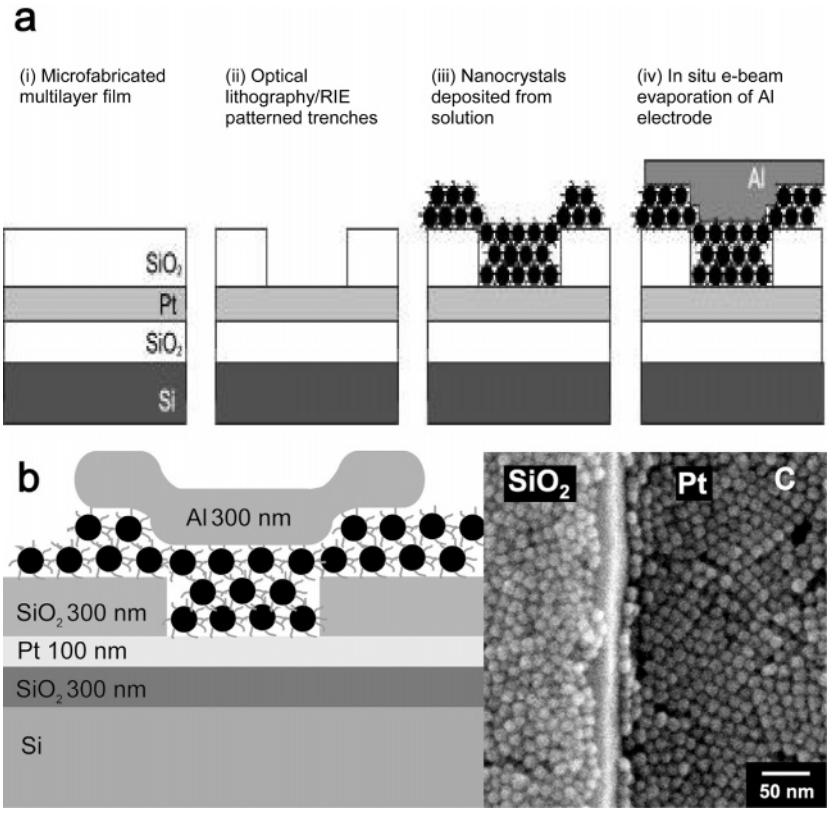

Figure 10. Schematic representation (a) of device fabrication and (b) of the device cross section. (c) SEM image of multilayers of the deposited Fe_xO nanoparticles covering a 0.3 μm gap of rectangular shape. Regions with hexagonal ordering are clearly visible.

This process allows parallel fabrication of many independent devices on a single wafer. In these experiments, two different types of devices were investigated—devices containing cubic nanocrystals (11 nm edge length, 5% SD, see Figure 5a) and 14 nm faceted particles (12% SD, see SEM in Figure 10c). For both types of device, there is neither aggregation of individual nanoparticles nor crystal growth within the superlattices during the 450 °C anneal, as confirmed by independent annealing experiments and X-ray powder spectroscopy. The annealing experiments also confirm that initial particles mainly composed of Fe_xO are completely transformed into magnetite and iron. Completed devices containing cubic particles were unusable due to either extremely high resistance (caused by too many nanocrystal layers) or electronic short-circuits between top and bottom electrode. A likely cause for this second type of failure is the strong self-assembly tendency of cubic nanocrystals (see Supporting Information, c and d). In contrast, devices formed of 14 nm faceted particles form thin, hexagonally packed multilayers which completely cover the Pt counter electrode (Figure 10c).

The conductivity of all measured nanocrystal devices decreases strongly with decreasing temperature, as illustrated by measurements of the zero-bias conductance ($G_{\text{zero bias}}$) of a 10 mm diameter device (Figure 11). Device conductivity was measured using both a four-probe direct current measurement (50 mV voltage bias) and a four-probe alternating current lock-in technique (11 Hz, 500 mV excitation). The conductivity of nanocrystal devices is governed by sequential electron tunneling through the array, and at low bias electrons can only surmount the significant electrostatic energy barrier (U) for tunneling between nanocrystals via thermal fluctuations. In this example, the dependence of $G_{\text{zero bias}}$ on T falls somewhere between a simple Arrhenius relationship ($G_{\text{zero bias}} \sim \exp[-U/k_BT]$, valid for uniformly sized particles with a single activation energy U) and a relationship appropriate for granular films with a broad size distribution ($G_{\text{zero bias}} \sim \exp[-(U^*/k_BT)^{-1/2}]$, where U^* is related to the average activation energy in the system). This observation seems reasonable in light of the nature of the nanocrystals used in these devices (i.e., 12% SD). Such intermediate situations between uniform and granular material have been previously discussed using a simplified model, assuming a normal distribution of particle sizes.[33] To estimate the activation energy in this system, the data of Figure 11a are fitted with an Arrhenius form, from which an energy $U \approx 120$ meV is calculated. This relatively high barrier is comparable with the charging energy of particles with a diameter of 2 nm arranged in a close-packed superlattice (nine nearest neighbors) and particles separated from each other by 2 nm (governed by interdigitating oleic acid molecules, $\epsilon_{\text{oleic acid}} \approx 2$).[34] As seen in Figure 11a, the device conductance decreases continuously with temperature, without any observable discontinuity at the Verwey transition, even through this phase transition is easily detected in ZFC or FC SQUID measurements (see Supporting Information Figure 10). The first-order Verwey phase transition in nanoscale magnetite has been previously observed in conductivity measurements of both particle arrays or in single particles (using scanning tunneling microscope) and by determination of the magnetic moment.

$$G_{\text{total}} \propto \sqrt{\frac{1}{2\Pi\sigma^2}} \int \exp\left[-\left(\frac{U-U_0}{4\sigma}\right)^2 - \frac{U}{k_BT}\right] dU \quad (1)$$

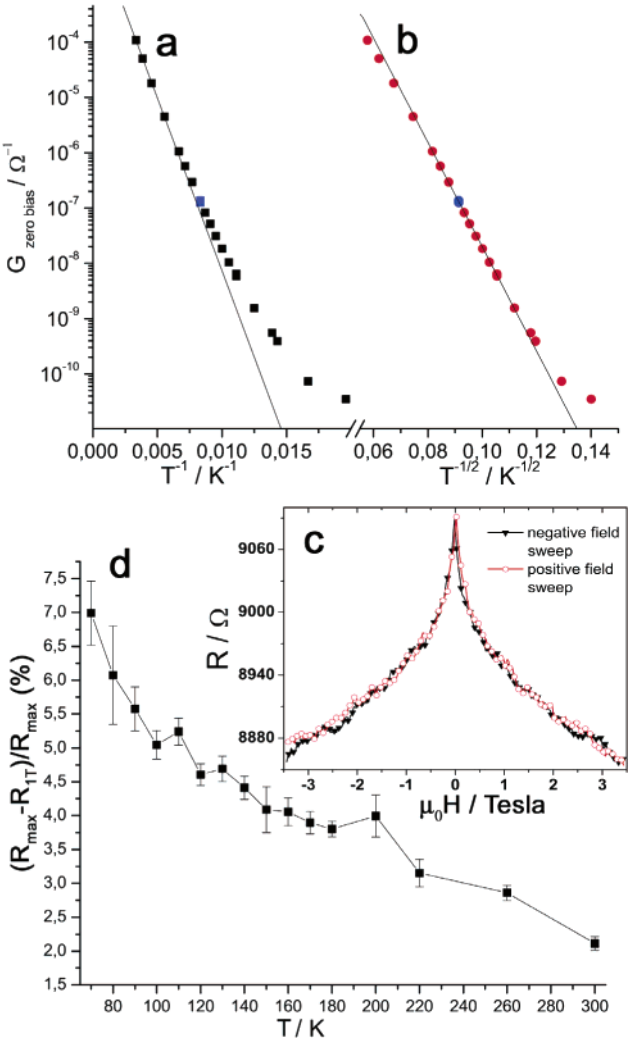

Figure 11. Plot of zero-bias conductivity, $G_{zero\ bias}$, vs (a) T^{-1} and (b) $T^{-1/2}$. (c) 300 K device resistance (50 mV bias) vs applied magnetic field. (d) Mean change in device resistance for applied fields of 0 and 1 T. Device magnetoresistance is unchanged for bias voltages up to $V_{bias} = 0.5$ V.

As the applied magnetic field H is increased from zero, device resistance drops sharply before slowing as H increases beyond ~0.25 T. A typical example of the dependence of device resistance on applied field (at 300 K and 50 mV bias) is shown in Figure 11c. The position of the device resistance maximum depends on the magnetic field sweep direction and correlates well with the ZFC and FC coercivity (ca. 200 Oe) of similarly annealed particles (see Supporting Information Figure 10). The gap between ZFC and FC at 300 K is due to a blocking temperature exceeding the measurement limit (at the longer measurement time scale of the SQUID).

The maximum device resistance change between applied fields of 0 and 1 T is 7% at 60 K and decreases monotonically with increasing temperature, shrinking to 2% at 300 K (Figure 11d). This percentage decrease is of a magnitude which can be understood in terms of increasing temperature-induced nanoparticle magnetic moment fluctuations. The smooth decrease in magnetoresistance with increasing temperature gives no hint of the Verwey phase transition in the nanocrystals comprising the device. In contrast to previous observations of a strong magnetoresistance decrease with increasing applied bias voltage,[33,81] our devices show little change for V_{bias} up to 0.5 V. Figure 11d plots the mean resistance change between applied fields of 0 and 1 T, for V_{bias} between −0.5 and 0.5 V (standard deviations are indicated by error bars in the graph).

Two surprising results from our analysis of the temperature- and magnetic-field dependence of the conductivity of devices formed of iron-based nanocrystals are the lack of an electronic signature of the Verwey phase transition and the anomalously high activation energy U for charge transport through the array. One possible explanation, which is consistent with these observations, is that the conductivity of the nanocrystalline material is dominated by incorporated iron. According to the previously discussed structural characterization of annealed samples, we assume that annealing promotes an Fe/Fe_3O_4 core/shell structure. A nanocrystal core of high-quality magnetite will display a pronounced change in magnetization at the Verwey transition temperature and will act to guide the magnetization orientation of the surrounding Fe shell. The tunneling rate for electrons moving between nanocrystals is not influenced by the magnetization change of the Fe_3O_4 core at the Verwey transition, but rather only by the magnetization of the Fe shell. If the electronic states of the Fe shell and Fe_3O_4 core are sufficiently decoupled, this would also lead to an increased activation energy U for electrons tunneling into Fe shell states. Further experiments such as characterization of nanocrystal devices annealed at different temperatures would shed more light on why, in this case, we observe a clear Verwey transition in nanocrystal magnetization but not magnetoresistance.

Conclusions

We have investigated the synthetic parameters that influence the size, structure, and composition of iron oxide nanocrystals prepared via iron salt and iron organometallic precursors. The $Fe_xO/Fe_3O_4/Fe_2O_3$ nanocrystal system proved to be a rich resource from which to derive insight into the behavior and reactivity of iron with oxygen, and the electronic and magnetic properties that result. The preparation of pure wüstite nanocrystals by decomposition methods is complicated by the metastable nature of wüstite. First, the disproportionation promotes aggregation of the particles; second, nearly all the investigated samples incorporate seeds of magnetite. Furthermore, the stability against oxidation of wüstite nanocrystals is highly size-dependent. Particles smaller than 10 nm are easily oxidized to magnetite or maghemite under ambient conditions. The best synthetic results were obtained either with the decomposition of iron(II) acetate or with a selective oxidation method by decomposition of iron pentacarbonyl in the presence of pyridine *N*-oxide. The oxidation and the product are hereby dependent on the concentration of the oxidizer pyridine *N*-oxide and surfactant oleic acid or lauric acid, which underlie a preliminary acid−base equilibrium, probably determining the free concentration of the oxidizer. This reaction is an example of a controlled oxidation with means of an organic oxidizer in nanoscale syntheses and yields cubic or spherical nanocrystals of about 10−13 nm. Although the reported syntheses are not able to deliver phase-pure wüstite, the product can be used as a precursor for magnetite or maghemite particles. Furthermore, the cubic sample readily assembles in three-dimensional superlattices, which can be directed and controlled by an external magnetic field. The magnetic properties can be steadily changed by controlled annealing or oxidation of the wüstite phase.

Intermediate composites display exchange coupling caused by growing or diminishing interfaces between wüstite and magnetite. Superparamagnetism dominated the magnetic behavior of all samples down to about 100 K. Thereafter, Mössbauer spectroscopy gave insight into the behavior and relative compositions of Fe^{2+} and Fe^{3+} in the different oxygen coordination environments. By measuring far below the blocking temperature of the samples, spin fluctuations are completely frozen relative to the characteristic measuring time of the Mössbauer technique, and this permitted the observation of the presence of a spin-glass-like, amorphous Fe_xO/Fe_3O_4 interfacial phase.

Iron oxide nanocrystal multilayers were self-assembled onto a patterned wafer and, following device fabrication, the electronic conduction was measured. It was found that nanocrystal core of high-quality magnetite will display a pronounced change in magnetization at the Verwey transition temperature and will act to guide the magnetization orientation of the surrounding Fe shell. The tunneling rate for electrons moving between nanocrystals is influenced not by the magnetization change of the Fe_3O_4 core at the Verwey transition, but by the magnetization of the Fe shell.

Acknowledgment. Our research team would like to thank Dr. Ali Afzali (IBM, T.J. Watson Research Center) for DSC and TGA measurements, and Dr. David R. Medeiros for the GC−MS measurements. This work was supported primarily by the MRSEC Program of the National Science Foundation under Award No. DMR-0213574 at Columbia University, in part by the U.S. Department of Energy, Office of Basic Energy Sciences, through the Catalysis Futures Grant DE-FG02-03ER15463, and in part under the MRSEC NSF Award No. DMR-0074537 at Villanova University. F.X.R. was supported in part by the DARPA Metamaterials initiative under ONR Contract No. N00014-01-C-0320.

Supporting Information Available: Discussion of the additional experimental parameters and size evolution of iron oxide nanocrystals up to 40 nm; X-ray diffraction studies of composition and electron microscopy of individual and superlattices of cubic nanocrystals; TEM and SAED images for wüststite particles in the size range 15−26 nm; FT-IR spectra of reaction solutions; full temperature-dependent Mössbauer spectra of the four investigated samples; coercivity vs temperature of 12 nm cubic FeO nanocrystals; DSC curve of spherical 10 nm wüstite nanocrystals; optical microscope images of substrate prepared for conductivity measurements; and SQUID measurements (ZFC and FC) of faceted FeO particle. This material is available free of charge via the Internet at http://pubs.acs.org.

JA046808R